J. Fluid Mech. (2019), *vol.* 875, *pp.* 725–757.
doi:10.1017/jfm.2019.422

Bifurcation analysis and frequency prediction in shear-driven cavity flow

Y. Bengana[1], J.-Ch. Loiseau[2], J.-Ch. Robinet[2] and L. S. Tuckerman[1,†]

[1]Laboratoire de Physique et Mécanique des Milieux Hétérogènes (PMMH), CNRS; ESPCI Paris, PSL Research University; Sorbonne Université; Univ. Paris Diderot, 75005 Paris, France

[2]Laboratoire DynFluid, Arts et Métiers ParisTech, 75013 Paris, France

(Received 1 November 2018; revised 10 May 2019; accepted 17 May 2019)

A comprehensive study of the two-dimensional incompressible shear-driven flow in an open square cavity is carried out. Two successive bifurcations lead to two limit cycles with different frequencies and different numbers of structures which propagate along the top of the cavity and circulate in its interior. A branch of quasi-periodic states produced by secondary Hopf bifurcations transfers the stability from one limit cycle to the other. A full analysis of this scenario is obtained by means of nonlinear simulations, linear stability analysis and Floquet analysis. We characterize the temporal behaviour of the limit cycles and quasi-periodic state via Fourier transforms and their spatial behaviour via the Hilbert transform. We address the relevance of linearization about the mean flow. Although here the nonlinear frequencies are not very far from those obtained by linearization about the base flow, the difference is substantially reduced when eigenvalues are obtained instead from linearization about the mean and in addition, the corresponding growth rate is small, a combination of properties called RZIF (real zero imaginary frequency). Moreover growth rates obtained by linearization about the mean of one limit cycle are correlated with relative stability to the other limit cycle. Finally, we show that the frequencies of the successive modes are separated by a constant increment.

Key words: bifurcation, free shear layers, vortex shedding

1. Introduction

We consider the incompressible shear-driven flow in a cavity, also known as open cavity flow. The first two-dimensional instability of the flow is localized along the shear layer delimiting the outer boundary layer above the cavity and also along the downstream side of the cavity (Sipp & Lebedev 2007; Sipp *et al.* 2010). This instability relies essentially on two mechanisms. First, the convectively unstable nature of the shear layer causes perturbations to grow as they travel downstream, essentially due to the Kelvin–Helmholtz mechanism. Once they impinge on the downstream corner of the cavity, the inner-cavity recirculating flow and the instantaneous pressure feedback provide the mechanisms by which these perturbations re-excite the upstream portion of the shear layer. At sufficiently high Reynolds numbers, the coupling of

† Email address for correspondence: laurette@pmmh.espci.fr

these mechanisms gives rise to a linearly unstable feedback loop. A similar unstable loop exists for compressible shear-driven cavity flows in which the instantaneous pressure feedback is replaced by upstream-propagating acoustic waves (Rossiter 1964; Rockwell & Naudascher 1978; Rowley, Colonius & Basu 2002; Gloerfelt 2009; Yamouni, Sipp & Jacquin 2013). The shear-driven open cavity flow has a number of applications in aeronautics (Yu 1977) and in industry, where it can serve as a mixing device (Chien, Rising & Ottino 1986).

Shear-driven instabilities in a cavity are often preceded by centrifugal instabilities as the Reynolds number is increased. The two are easy to distinguish since the shear-driven instabilities lead to streamwise travelling waves while the centrifugal instabilities lead to steady oscillations which are spanwise periodic (away from rigid boundaries if these are present). These spanwise oscillations are observed in simulations (Aidun, Triantafillopoulos & Benson 1991; Theofilis, Duck & Owen 2004; Picella *et al.* 2018) and in experiments (Shankar & Deshpande 2000; Faure *et al.* 2007, 2009; Douay, Pastur & Lusseyran 2016). This could make the two-dimensional (spanwise-independent) case seem academic. However, because the spanwise oscillations are of low amplitude and are mainly located inside the cavity, they have a minimal effect on the subsequent development of the flow for this range of Reynolds numbers. As the Reynolds number is further increased, shear-driven instabilities occur, leading to states resembling streamwise travelling waves (Basley *et al.* 2013). The resulting streamwise wavelengths and temporal frequencies are very similar to those observed in the spanwise-independent case, but the critical Reynolds numbers are different (Basley *et al.* 2011, 2013). Experiments (Rossiter 1964; Rockwell 1977; Rockwell & Naudascher 1978; Basley *et al.* 2011, 2013) have shown that over a large range of aspect ratios, the frequency of the dominant mode is approximated quite well by a spanwise-independent approach. Rockwell (1977), Rockwell & Naudascher (1978) showed that in a square cavity with a short spanwise extent, the mode produced has a streamwise wavelength which is approximately half the cavity length and a temporal period which is approximately one, in units of the cavity length and imposed velocity. A closely related case is that of the double cavity, in which a second cavity is located above the layer of imposed streamwise flow. The numerical simulations of Tuerke *et al.* (2017) have shown that for both single and double cavities, periodic dynamics appears in the Reynolds number range between 4000 and 4300, with a dominant Strouhal number close to one. This is consistent with our numerical results.

The two-dimensional shear-driven cavity has served multiple theoretical modelling purposes over the past decade, such as in optimal control, reduced-order modelling (Barbagallo, Sipp & Schmid 2009; Loiseau & Brunton 2018) and dynamic mode decomposition (Schmid 2010). Despite its use as a representative test case for complex nonlinear dynamics in fluid mechanics, an extensive analysis of the first few bifurcations experienced by the shear-driven cavity flow has never been carried out. The primary aim of the present work is to fill this gap. We have been able to determine the first primary and secondary bifurcations experienced by the flow and to draw the associated bifurcation diagram. The combined use of nonlinear direct numerical simulation, linear stability analysis and Floquet analysis then enabled us to investigate the stability of the various solution branches. More specifically, we have studied two limit cycles whose relative stability is mediated by an unstable quasi-periodic state. Our study is thus complementary to those of Sipp & Lebedev (2007) and Meliga (2017), each of which treats one of the two limit cycles covered in this study. Another relevant numerical study is that of Tiesinga, Wubs & Veldman

(2002), who conducted a bifurcation analysis of the two-dimensional lid-driven cavity which, in the parameter range of our study, behaves very similarly to the open cavity. Oscillations along the top of the cavity are, of course, ruled out, but the oscillations that travel down the downstream side of the cavity are quite similar in appearance and in behaviour. As in our case, two limit cycles and an intermediate quasi-periodic state are found. Because of the viscous damping by the lid, the critical Reynolds numbers are approximately twice those for the open cavity (Poliashenko & Aidun 1995; Fortin *et al.* 1997).

A second theme of our investigation, also previously addressed by Sipp & Lebedev (2007) and Meliga (2017), is the relevance of linearization about the mean flow. For a fully developed limit cycle, nonlinear interactions contribute to the mean flow, leading to a deviation from the base flow called the distortion. In this way, the mean flow inherits information from the nonlinearities (Maurel, Pagneux & Wesfreid 1995; Zielinska *et al.* 1997). From this comes the idea to linearize about the mean flow, despite the fact that the mean flow is not a solution of the stationary Navier–Stokes equations. Although the empirical use of mean flows to study nonlinear dynamics is long standing (Malkus 1956; Stuart 1958; Morris 1976), quantitative computations and comparisons are more recent, and primarily for the wake of a circular cylinder (Hammond & Redekopp 1997; Pier 2002; Barkley 2006; Mittal 2008). When successful, this procedure leads to an eigenvalue whose imaginary part reproduces very well the frequency of the periodic orbit, even quite far from its threshold. Moreover, the real part of this eigenvalue is close to zero (Barkley 2006), which would be called marginal stability if the linearization were about the base flow. This property was named RZIF (a mnemonic for real zero imaginary frequency) by Turton, Tuckerman & Barkley (2015). An extension of RZIF called SCM (for self-consistent model) has been proposed by Mantič-Lugo, Arratia & Gallaire (2014, 2015), in which the mean flow is computed, not as an average of the full time-dependent flow, but precisely so that the RZIF property is satisfied, i.e. such that the mean flow is marginally stable. Neither RZIF nor SCM are always valid; counterexamples have been found for regimes in thermosolutal convection by Turton *et al.* (2015) and Bengana (2019). Other flows for which these properties or models have been tested are the compressible flow in the wake of a cylinder (Fani *et al.* 2018) and counter-rotating Taylor–Couette flow (Bengana & Tuckerman 2019). Linearization about the mean flow has been applied to understanding the temporal spectra of turbulent flows (McKeon & Sharma 2010; Hwang & Cossu 2010; Beneddine *et al.* 2016; Symon *et al.* 2018).

The paper is organized as follows: § 2 introduces the configuration of the shear-driven cavity flow and the governing equations and the tools for the various analyses we have performed, i.e. linearization about the base and the mean flows, Floquet analysis, the temporal Fourier transform and the spatial Hilbert transform. Our results concerning the bifurcation scenario for this flow are presented in § 3, more specifically two limit cycles produced by primary Hopf bifurcations and whose relative stability is mediated by an unstable quasi-periodic state produced by secondary bifurcations. In § 4, we discuss linearization about the mean flow for both limit cycles, as well as the formula of Rossiter (1964). We summarize our conclusions in § 5.

2. Governing equations and numerical methods

2.1. *Problem definition*

The configuration considered is the two-dimensional incompressible viscous shear-driven flow of a Newtonian fluid over an open cavity with equal length and depth

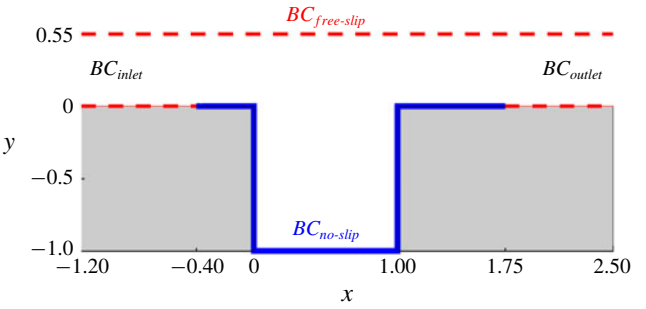

FIGURE 1. (Colour online) Geometry of our study. At the inlet (BC_{inlet}) a uniform unit velocity ($u = 1$; $v = 0$) is imposed. Dashed red line: free-slip condition ($BC_{free\text{-}slip}$). Thick blue line: no-slip boundary condition ($BC_{no\text{-}slip}$). A free-outflow boundary condition is imposed at the outlet.

shown in figure 1. This configuration is the same as that considered by Sipp & Lebedev (2007) and Barbagallo *et al.* (2009), or more recently by Meliga (2017). We use the unperturbed upstream velocity U_∞, the cavity length L and the resulting advective time L/U_∞ to non-dimensionalize the variables. The dynamics of the flow is governed by the incompressible Navier–Stokes equations

$$\left.\begin{aligned} \frac{\partial \boldsymbol{U}}{\partial t} &= -\boldsymbol{\nabla} P + \frac{1}{Re}\boldsymbol{\nabla}^2 \boldsymbol{U} - \boldsymbol{\nabla}\cdot(\boldsymbol{U}\otimes\boldsymbol{U}), \\ 0 &= \boldsymbol{\nabla}\cdot\boldsymbol{U}, \end{aligned}\right\} \tag{2.1}$$

where $\boldsymbol{U}(\boldsymbol{x}, t) = (U, V)^{\mathrm{T}}$ and P are the velocity and pressure fields. The Reynolds number Re is defined as

$$Re = \frac{U_\infty L}{\nu}, \tag{2.2}$$

where ν is the kinematic viscosity of the fluid, and will range between $Re = 4000$ and 5000. The boundary conditions, illustrated in figure 1, are

$$\left.\begin{aligned} \boldsymbol{U} &= \boldsymbol{e_x} \quad \text{on } BC_{inlet}, \\ \boldsymbol{U} &= \boldsymbol{0} \quad \text{on } BC_{no\text{-}slip}, \\ \partial_y U = V &= 0 \quad \text{on } BC_{free\text{-}slip}, \\ \partial_x \boldsymbol{U} &= \boldsymbol{0} \quad \text{on } BC_{outlet}. \end{aligned}\right\} \tag{2.3}$$

The boundary conditions at the inlet and along the wall are crucial. The flow is given a uniform profile at the inlet and develops a boundary layer structure as it advances downstream. The instability occurs where the boundary layer reaches the upstream corner of the cavity and it is the thickness of the boundary layer at this point that controls the details of the transition. When free-slip conditions are imposed on the wall close to the inlet, then a boundary layer of an appropriate thickness develops over a shorter distance than would be the case if no-slip conditions were used over the entire wall. A shorter domain can be used, making the calculation more economical.

The Navier–Stokes equations are solved using the incompressible flow solver NEK5000 (Fischer, Lottes & Kerkemeir 2008) which is based on the spectral element

method. A $\mathbb{P}_N - \mathbb{P}_{N-2}$ formulation has been used: the velocity field is discretized using Nth-order Lagrange interpolants defined on the Gauss–Legendre–Lobatto quadrature points as basis and trial functions while the pressure field is discretized using Lagrange interpolants of degree $N - 2$ defined on the Gauss–Legendre quadrature points. Finally, time integration is performed using the BDF3/EXT3 scheme: integration of the viscous term relies on backward differentiation while the convective terms are integrated explicitly using a third-order accurate extrapolation. In practice, the polynomial degree was set to $N = 6$ while the computational domain was discretized using 4000 spectral elements. The resulting mesh refinement is thus similar to that used in Sipp & Lebedev (2007).

2.2. *Base flow and linearization*

A base flow $\boldsymbol{U}_b(\boldsymbol{x})$ is a solution of the stationary Navier–Stokes equations

$$\left.\begin{aligned} 0 &= -\boldsymbol{\nabla} P_b + \frac{1}{Re}\nabla^2 \boldsymbol{U}_b - \boldsymbol{\nabla}\cdot(\boldsymbol{U}_b \otimes \boldsymbol{U}_b), \\ 0 &= \boldsymbol{\nabla}\cdot\boldsymbol{U}_b, \end{aligned}\right\} \tag{2.4}$$

with the boundary conditions again given by (2.3). Various techniques can be used to compute the base flow $\boldsymbol{U}_b(\boldsymbol{x})$. Because of its simplicity, the selective frequency damping (SFD) technique initially proposed by Åkervik *et al.* (2006) has been used; see also Jordi, Cotter & Sherwin (2014, 2015), Cunha, Passaggia & Lazareff (2015).

Once the equilibrium $\boldsymbol{U}_b(\boldsymbol{x})$ has been computed, we determine its linear stability. To do so, we consider an infinitesimal perturbation $\boldsymbol{u}(\boldsymbol{x}, t)$ to the base flow $\boldsymbol{U}_b$, whose dynamics is governed by the linearized Navier–Stokes equations

$$\left.\begin{aligned} \frac{\partial \boldsymbol{u}}{\partial t} &= -\boldsymbol{\nabla} p + \frac{1}{Re}\nabla^2 \boldsymbol{u} - \boldsymbol{\nabla}\cdot(\boldsymbol{U}_b \otimes \boldsymbol{u} + \boldsymbol{u} \otimes \boldsymbol{U}_b), \\ 0 &= \boldsymbol{\nabla}\cdot\boldsymbol{u}. \end{aligned}\right\} \tag{2.5}$$

The boundary conditions are the homogeneous version of (2.3), i.e. we now prescribe a zero velocity profile at the inlet.

$$\left.\begin{aligned} \boldsymbol{u} &= \boldsymbol{0} \quad \text{on } BC_{inlet}, \\ \boldsymbol{u} &= \boldsymbol{0} \quad \text{on } BC_{no\text{-}slip}, \\ \partial_y u = v &= 0 \quad \text{on } BC_{free\text{-}slip}, \\ \partial_x \boldsymbol{u} &= \boldsymbol{0} \quad \text{on } BC_{outlet}. \end{aligned}\right\} \tag{2.6}$$

Solutions to (2.5)–(2.6) are of the form $\boldsymbol{u}(\boldsymbol{x}, t) = \hat{\boldsymbol{u}}(\boldsymbol{x})\mathrm{e}^{(\sigma+\mathrm{i}\omega)t} + \text{c.c.}$, $p(\boldsymbol{x}, t) = \hat{p}(\boldsymbol{x})\mathrm{e}^{(\sigma+\mathrm{i}\omega)t} + \text{c.c.}$, from which we obtain the eigenvalue problem

$$\left.\begin{aligned} (\sigma + \mathrm{i}\omega)\hat{\boldsymbol{u}} &= \mathcal{L}_{U_b}\hat{\boldsymbol{u}}, \\ 0 &= \boldsymbol{\nabla}\cdot\hat{\boldsymbol{u}}, \end{aligned}\right\} \tag{2.7}$$

where $\mathcal{L}_{U_b}$ is the Jacobian of the Navier–Stokes equations linearized around $\boldsymbol{U}_b$,

$$\mathcal{L}_{U_b}\hat{\boldsymbol{u}} \equiv -\boldsymbol{\nabla}\hat{p} + \frac{1}{Re}\nabla^2\hat{\boldsymbol{u}} - \boldsymbol{\nabla}\cdot(\boldsymbol{U}_b \otimes \hat{\boldsymbol{u}} + \hat{\boldsymbol{u}} \otimes \boldsymbol{U}_b). \tag{2.8}$$

The stability of the base flow is determined by the sign of the real part σ of the leading eigenvalue, which is the growth rate of the perturbation. If σ crosses zero for an eigenvalue with non-zero imaginary part ω, then a Hopf bifurcation leads to a limit cycle whose frequency at onset is ω. In our case, the base flow undergoes a first Hopf bifurcation at $Re_2 = 4126$, leading to a limit cycle LC_2 and a second Hopf bifurcation at $Re_3 = 4348$ gives rise to LC_3.

We computed the leading eigenvalues and eigenvectors using a time-stepper approach; see, e.g. Edwards *et al.* (1994). Our stability calculation typically used a Krylov subspace of dimension $K = 256$ and a sampling period $\Delta T = 10^{-3}$ non-dimensional time units. Eigenvalues were considered to be converged if the residual obtained from the Arnoldi decomposition was below 10^{-6}.

2.3. *Mean flow and linearization*

At the threshold of a Hopf bifurcation, linearization about the base flow leads to an eigenvalue whose real part is zero and whose imaginary part is the frequency of the limit cycle which is produced. As the Reynolds number is increased and the limit cycle develops nonlinearly and deviates from the base flow, eigenvalues obtained by linearization about the base flow no longer correspond to the properties of the limit cycle. However, linearization about the mean flow often leads to an eigenvalue whose imaginary part is closer to the nonlinear frequency.

We consider a Reynolds decomposition of the instantaneous flow field, i.e.

$$\boldsymbol{U}(\boldsymbol{x}, t) = \overline{\boldsymbol{U}}(\boldsymbol{x}) + \boldsymbol{u}(\boldsymbol{x}, t), \tag{2.9}$$

where $\overline{\boldsymbol{U}}(\boldsymbol{x})$ is the mean flow and $\boldsymbol{u}(\boldsymbol{x}, t)$ is the zero-mean fluctuation. Introducing this decomposition into the Navier–Stokes equations and averaging shows that $\overline{\boldsymbol{U}}$ is governed by the Reynolds averaged Navier–Stokes (RANS) equations

$$\left.\begin{aligned} 0 = -\boldsymbol{\nabla}\overline{P} + \frac{1}{Re}\boldsymbol{\nabla}^2\overline{\boldsymbol{U}} - \boldsymbol{\nabla}\cdot(\overline{\boldsymbol{U}}\otimes\overline{\boldsymbol{U}}) - \boldsymbol{\nabla}\cdot(\overline{\boldsymbol{u}\otimes\boldsymbol{u}}),\\ 0 = \boldsymbol{\nabla}\cdot\overline{\boldsymbol{U}}, \end{aligned}\right\} \tag{2.10}$$

with inhomogeneous boundary conditions (2.3). The presence of the Reynolds stress tensor $\overline{\boldsymbol{u}\otimes\boldsymbol{u}}$ of the fluctuation means that these equations are not closed. We compute the mean flow $\overline{\boldsymbol{U}}(\boldsymbol{x})$ of a period-T limit cycle by carrying out a full nonlinear simulation via (2.1), (2.3) and time averaging,

$$\overline{\boldsymbol{U}}(\boldsymbol{x}) = \frac{1}{T}\int_0^T \boldsymbol{U}(\boldsymbol{x}, t)\,\mathrm{d}t. \tag{2.11}$$

The equations governing the dynamics of the fluctuation $\boldsymbol{u}(\boldsymbol{x}, t)$ are obtained by substituting $\overline{\boldsymbol{U}} + \boldsymbol{u}$ for $\boldsymbol{U}$ into (2.1) and subtracting (2.10), leading to

$$\left.\begin{aligned} \frac{\partial\boldsymbol{u}}{\partial t} = -\boldsymbol{\nabla}p + \frac{1}{Re}\boldsymbol{\nabla}^2\boldsymbol{u} - \boldsymbol{\nabla}\cdot(\overline{\boldsymbol{U}}\otimes\boldsymbol{u} + \boldsymbol{u}\otimes\overline{\boldsymbol{U}}) - \underbrace{\boldsymbol{\nabla}\cdot(\boldsymbol{u}\otimes\boldsymbol{u} - \overline{\boldsymbol{u}\otimes\boldsymbol{u}})}_{\boldsymbol{f}},\\ 0 = \boldsymbol{\nabla}\cdot\boldsymbol{u}, \end{aligned}\right\} \tag{2.12}$$

with homogeneous boundary conditions (2.6). The equations differ from the linearized Navier–Stokes equations by the presence of $\boldsymbol{f}$. The term $\boldsymbol{\nabla}\cdot(\boldsymbol{u}\otimes\boldsymbol{u})$, is the usual

quadratic interaction term neglected in base flow linear stability analyses. The term $\boldsymbol{\nabla}\cdot(\overline{\boldsymbol{u}\otimes\boldsymbol{u}})$ is the divergence of the Reynolds stress tensor of the fluctuation.

Studies carrying out mean flow stability analyses discard $\boldsymbol{f}$, leading to the linearized equations

$$\left.\begin{aligned}\frac{\partial \boldsymbol{u}}{\partial t} &= -\boldsymbol{\nabla} p + \frac{1}{Re}\nabla^2\boldsymbol{u} - \boldsymbol{\nabla}\cdot(\boldsymbol{u}\otimes\overline{\boldsymbol{U}} + \overline{\boldsymbol{U}}\otimes\boldsymbol{u}),\\ 0 &= \boldsymbol{\nabla}\cdot\boldsymbol{u}.\end{aligned}\right\} \tag{2.13}$$

Using once again a normal mode ansatz, this set of equations is reduced to the eigenvalue problem

$$\left.\begin{aligned}(\sigma + \mathrm{i}\omega)\hat{\boldsymbol{u}} &= \mathcal{L}_{\overline{U}}\hat{\boldsymbol{u}},\\ 0 &= \boldsymbol{\nabla}\cdot\hat{\boldsymbol{u}},\end{aligned}\right\} \tag{2.14}$$

where $\mathcal{L}_{\overline{U}}$ is now the Navier–Stokes operator linearized around the mean flow, with $\overline{\boldsymbol{U}}$ substituted for $\boldsymbol{U}_b$ in (2.8).

Although the mean flow is not an equilibrium solution of the Navier–Stokes solution, this approach has proved unexpectedly successful in characterizing the frequencies of the full nonlinear solutions of the Navier–Stokes equations. (For a counter-example, however, see Turton *et al.* (2015).) Various theoretical overlapping justifications have been proposed for dropping or modelling $\boldsymbol{f}$ in (2.12), such as:

(i) The quadratic interaction of the fluctuation with itself is small and its temporal mean does not appear in a linear stability analysis (Barkley 2006; Mantič-Lugo *et al.* 2014, 2015).

(ii) The terms can be treated via an expansion in the distance from the threshold (Sipp & Lebedev 2007).

(iii) The instantaneous Reynolds stress tensor $\boldsymbol{u}\otimes\boldsymbol{u}$ is approximately equal to its temporal average $\overline{\boldsymbol{u}\otimes\boldsymbol{u}}$ so that they almost cancel out (Turton *et al.* 2015); see also § 4.2.

(iv) The resolvent operator $(\mathrm{i}\omega - \mathcal{L}_{\overline{U}})^{-1}$ is sharply peaked or of low rank. This implies that its action on any vector, including $\boldsymbol{f}$, is approximately a projection onto the leading mode of the resolvent. The purpose of this procedure is not to eliminate $\boldsymbol{f}$, but to approximate it as a scalar multiple of the leading resolvent mode, and then to treat $\boldsymbol{f}$ as a forcing input (McKeon & Sharma 2010; Hwang & Cossu 2010; Beneddine *et al.* 2016; Symon *et al.* 2018).

2.4. *Floquet analysis*

Our study of the shear-driven cavity focuses on two limit cycles, denoted by LC_2 and LC_3, created by primary Hopf bifurcations and destabilized via secondary bifurcations. Floquet analysis will be used to characterize this destabilization. The dynamics of an infinitesimal perturbation $\boldsymbol{u}(\boldsymbol{x}, t)$ evolving in the vicinity of a T-periodic limit cycle $\boldsymbol{U}(\boldsymbol{x}, t)$ is governed by the linearized Navier–Stokes equations

$$\left.\begin{aligned}\frac{\partial \boldsymbol{u}}{\partial t} &= \mathcal{L}_{U(t)}\boldsymbol{u},\\ 0 &= \boldsymbol{\nabla}\cdot\boldsymbol{u},\end{aligned}\right\} \tag{2.15}$$

with homogeneous boundary conditions (2.6). This set of equations is non-autonomous, as the operator $\mathcal{L}_{U(t)}$ is T-periodic. Solutions to (2.15) are of the Floquet form

$$\boldsymbol{u}(\boldsymbol{x}, t) = \hat{\boldsymbol{u}}(\boldsymbol{x}, t)\mathrm{e}^{(\sigma_F + \mathrm{i}\omega_F)t} + \text{c.c.}, \tag{2.16}$$

where $\hat{\boldsymbol{u}}(\boldsymbol{x}, t)$ are the T-periodic Floquet modes and $(\sigma_F + \mathrm{i}\omega_F)$ the Floquet exponents. The stability of $\boldsymbol{U}(t)$ is determined by the Floquet multipliers

$$\mu = \mathrm{e}^{(\sigma_F + \mathrm{i}\omega_F)T}. \tag{2.17}$$

If the moduli of the Floquet multipliers are smaller than one, perturbations will decay exponentially fast and the orbit is stable. On the other hand, if at least one of the Floquet multipliers has a modulus greater than one, then that perturbation will grow exponentially and the orbit is unstable; see, e.g. Barkley & Henderson (1996) and Gioria *et al.* (2009). In our study the Floquet exponents are complex and the imaginary part ω_F of the Floquet exponent is the argument (angle) of the Floquet multiplier. The presence of an imaginary part leads to quasi-periodic behaviour. More details and results are shown in § 3.4.

2.5. *Edge state technique for computing the unstable quasi-periodic state*

As will be shown in § 3, there is a range of Reynolds numbers over which limit cycles LC_2 and LC_3 co-exist. In phase space, on the boundary between the basins of attraction of these limit cycles, is an unstable quasi-periodic state QP. (More specifically, QP is an edge state, meaning that within the boundary, trajectories are attracted to it.) In order to compute QP, we use the same technique as in Itano & Toh (2001) or Duguet, Willis & Kerswell (2008) for the laminar–turbulent edge state. In such cases, whether a trajectory evolves towards a turbulent or laminar state depends on the initial condition. Some initial conditions evolve directly to turbulence, others decay directly to the laminar state. By appropriately weighting turbulent and laminar solutions, an initial condition can be constructed so that the resulting trajectory converges to and remains a long time on the edge state before diverging towards one of these two attractors.

In our problem, a quasi-periodic state separates the two stable limit cycles LC_2 and LC_3. Therefore we construct a weighted sum of the two, seeking an initial condition $\boldsymbol{U}(\boldsymbol{x}, 0)$ that will evolve after some time to QP and then remain as long as possible before eventually converging to either limit cycle. Using the same bisection technique as in Lopez *et al.* (2017), this initial condition is given by

$$\boldsymbol{U}(\boldsymbol{x}, t) = \alpha \boldsymbol{U}_{LC_2} + (1 - \alpha)\boldsymbol{U}_{LC_3}. \tag{2.18}$$

For $\alpha = 1$, the initial condition is LC_2 and for $\alpha = 0$, it is LC_3. For each Reynolds number considered, we successively delimit an interval of α by bisection to capture the quasi-periodic state. As an illustration, we plot in figure 2 the time evolution of streamwise velocity recorded by a probe located at $(x_1, y_1) = (1.2, 0.2)$ for $\alpha =$ 0.47562027 and 0.47562256. A slight difference in α will bring the system after a long transient regime to either LC_2 or LC_3.

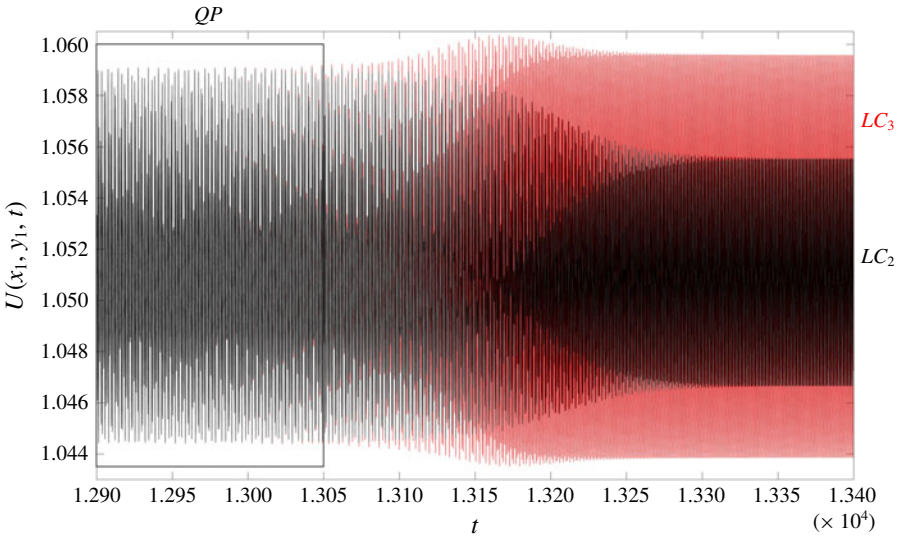

FIGURE 2. (Colour online) Time traces of streamwise velocity at $Re = 4460$ for two simulations. The initial condition of the simulation is (2.18). For $\alpha = 0.47562027$ the system evolves towards LC_2, shown as the black curve. For $\alpha = 0.47562256$ it evolves towards LC_3, shown as the higher-amplitude red curve.

2.6. *Standard deviation*

To construct the bifurcation diagram, we seek an appropriate measure of the oscillation amplitude as a function of Re. Time series from limit cycles LC_2 and LC_3 are shown in figures 2 and 3(*c*). Their amplitudes are easily obtained by measuring the maxima in a time series or the fundamental peak in the temporal Fourier spectrum. In contrast to these, which have maxima of constant amplitudes, the quasi-periodic state existing in the overlap region has maxima of varying heights as shown in figures 2 and 3(*b*). To extract a single amplitude in their study of the cubic lid-driven cavity, Lopez *et al.* (2017) used the standard deviation from the mean flow, defined as

$$\xi(U) = \left[\frac{1}{N}\sum_{n=0}^{N}(U(x_1, y_1, t_n) - \overline{U}(x_1, y_1))^2\right]^{1/2}, \tag{2.19}$$

where $U(x_1, y_1, t_n)$ the streamwise velocity measured at $(x_1, y_1) = (1.2, 0.2)$ and at each instant t_n, N is the number of measurements in the time series and $\overline{U}(x_1, y_1)$ is the temporal mean. We used the edge state technique described in § 2.5 to compute a time series in which the QP is maintained for a long time. In figure 3(*d*), we show the standard deviation of the time series plotted in figure 3(*a*). The standard deviation is computed over all times of a sliding window containing fifty peaks. Once the deviation is computed, the window is shifted by ten peaks and we compute the deviation again over fifty peaks. Figure 3(*d*) shows two regimes of constant $\xi(U)$ corresponding to QP and LC_2, justifying the choice of $\xi(U)$ for the bifurcation diagram.

2.7. *Hilbert transform*

We use the Hilbert transform to obtain spatial characteristics of the flow. The Hilbert transform is a useful means of extracting the local amplitude and phase from a signal.

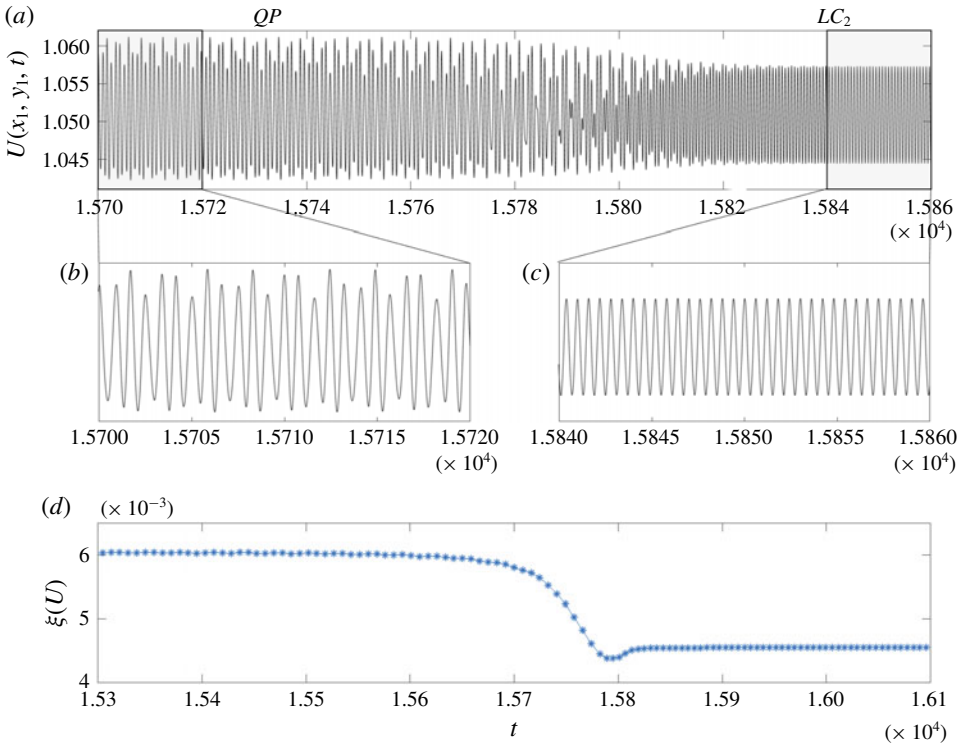

FIGURE 3. (Colour online) (*a*) Time series of streamwise velocity at $(x_1, y_1) = (1.2, 0.2)$ and $Re = 4580$ for a simulation with $\alpha = 0.829630407714844$. The regimes corresponding to QP and to LC_3 are shown in (*b*,*c*). (*d*) The standard deviation is computed by a sliding window.

A complex analytic signal $f_a(x)$ is constructed from real data $f(x)$. In contrast to a real signal that has negative and positive frequencies, f_a is complex and has only positive frequencies. This signal is obtained by

$$f_a(x) = f(x) + \mathrm{i}\mathcal{H}(f(x)). \tag{2.20}$$

The imaginary part $\mathcal{H}(f(x))$ is its Hilbert transform, defined by phase shifting the positive and negative frequencies of the original real signal by $-\pi/2$ and $\pi/2$, respectively. More details about the Hilbert transform can be found in Smith (2007). Equation (2.20) is written in polar form

$$f_a(x) = A(x)\mathrm{e}^{\mathrm{i}\Phi(x)}. \tag{2.21}$$

Thus we can extract the envelope (amplitude $A(x)$) and the phase $\Phi(x)$ from the analytic signal at each location, which is the main interest in using the Hilbert transform. We present the results in detail in § 3.3.

3. Bifurcation scenario

3.1. *Overview*

The flow over a shear-driven cavity at low Reynolds number consists of a free laminar shear layer and one large recirculation within the cavity. As we increase the Reynolds

number, the mixing layer is fed by the shear stress and its thickness develops over the cavity. As widely presented in several studies (Rockwell & Naudascher 1978), it is common to observe self-sustained oscillations in such configurations, in which the flow impacts on a wall. In figure 4(*a*) we show the bifurcation diagram over the range of Reynolds number $Re \in [4000, 5000]$. We represent the standard deviation from the mean of the streamwise velocity at a point as described in § 2.6. The standard deviation is computed over all times t_n of the time series corresponding to LC_2, LC_3 or QP. The line $\xi(U) = 0$ represents the solution of the stationary Navier–Stokes equations (base flow). We plot the stable and unstable states with bold and dashed curves, respectively.

The base flow is stable for $Re < Re_2$ where $Re_2 \approx 4126$ is the critical Reynolds number of the first Hopf bifurcation. This threshold is obtained by quadratic interpolation of amplitudes and differs by only 0.34 % from that found by Sipp & Lebedev (2007). Above this threshold, the base solution exists but is unstable. We observe a second Hopf bifurcation at $Re_3 \approx 4348$, also from quadratic interpolation of amplitudes, which agrees with the threshold measured by Meliga (2017), differing only by 0.005 %. These successive Hopf bifurcations lead after saturation by nonlinear interactions to two limit cycles which we name LC_2 and LC_3 because they display two or three maxima of the vertical velocity fluctuations, as will be shown in the next section.

Figure 4(*b*) shows the schematic phase portraits corresponding to the bifurcation diagram. The stable base flow (i) loses its stability through a primary Hopf bifurcation (ii) at Re_2 producing the limit cycle LC_2. (iii) Another primary Hopf bifurcation at Re_3 produces the limit cycle LC_3. (iv) A secondary subcritical Hopf bifurcation from LC_3 at Re_3' produces the quasi-periodic state QP, which moves (v) in phase space towards LC_2 until it undergoes another secondary subcritical Hopf bifurcation (vi) at Re_2' which destroys QP and destabilizes LC_2. Above Re_3', LC_3 is stable at least until $Re = 5000$. Another Hopf bifurcation and interesting dynamics occur above $Re = 5000$ but these will not be discussed in this paper.

This bifurcation diagram is very similar to that seen in the related configuration of a lid-driven cavity (Tiesinga *et al.* 2002). These authors observed two successive primary Hopf bifurcations leading to branches with different spatial characteristics. Stability is transferred from the first branch to the second via a secondary branch, which is itself created and destroyed via subcritical secondary Hopf bifurcations. The Reynolds numbers they report for the lid-driven cavity are $Re_2 \approx 8375$, $Re_3 \approx 8600$, $Re_3' = 8800$, $Re_2' = 9150$, quite close to twice those we find for the shear-driven cavity. Indeed, this is a classic scenario which occurs in many hydrodynamic configurations; see Kuznetsov (1998), Marques, Lopez & Shen (2002), Meliga, Gallaire & Chomaz (2012). Representing the dynamics by two complex amplitudes $r_2 e^{i\phi_2}$, $r_3 e^{i\phi_3}$, the dynamics is governed by the normal form,

$$\dot{r}_2 = r_2(\mu_2 - a_{22} r_2^2 - a_{23} r_3^2) \quad \dot{\phi}_2 = \omega_2 \tag{3.1a}$$

$$\dot{r}_3 = r_3(\mu_3 - a_{32} r_2^2 - a_{33} r_3^2) \quad \dot{\phi}_3 = \omega_3. \tag{3.1b}$$

where coefficients μ_j, a_{ij} depend on Re and a_{22} and a_{33} are positive. The diagrams of figure 4(*b*) are projections of the dynamics onto the (r_2, r_3) plane.

The base flow is shown in figure 5. Figure 5(*a*) shows a visualization of its spanwise vorticity $\Omega_b(x, y)$ over our domain for $Re = 4500$. The change in the mixing layer with increasing Re is not qualitatively visible on such a plot, so figure 5(*b*) presents profiles $\Omega_b(x = 0.5, y)$ at the midline for Reynolds numbers ranging from

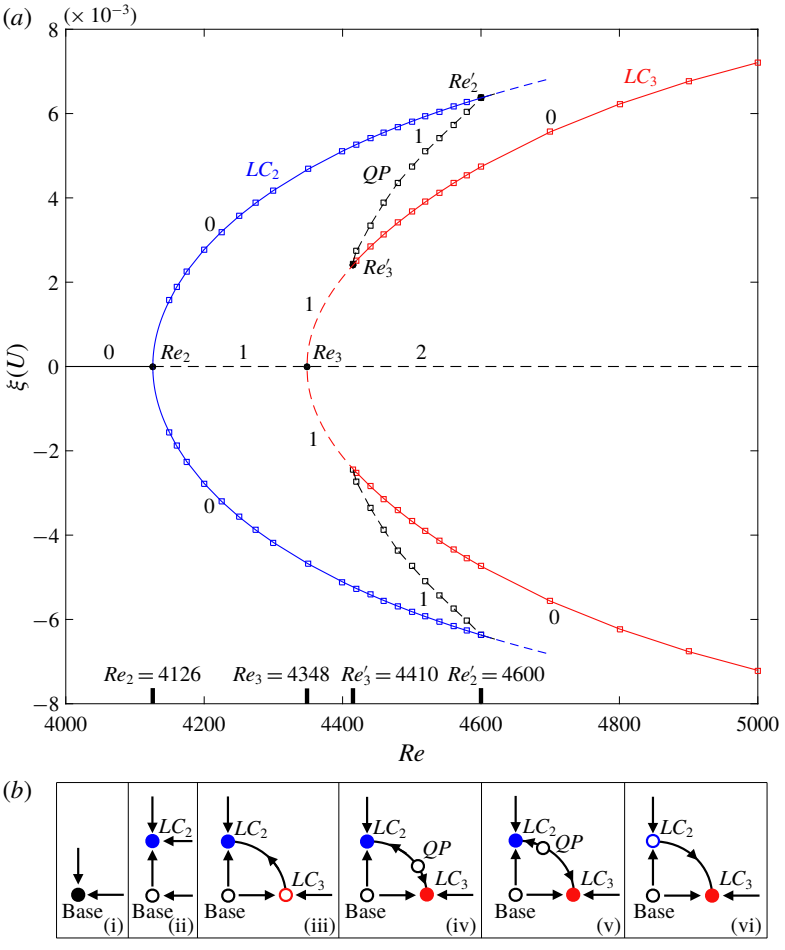

FIGURE 4. (Colour online) (*a*) Bifurcation diagram of the shear-driven cavity flow for $Re \in [4000, 5000]$. On the x-axis, we show the Reynolds number Re and on the y-axis the standard deviation from the mean of the streamwise velocity at one point. The bold dots on the curves and the thick ticks on the x-axis show the critical Reynolds numbers. The integers show the number of unstable directions (counting a complex conjugate pair as a single direction). We represent stable states by bold curves and unstable ones by dashed curves. The line $\xi(U) = 0$ indicates the stationary base flow. The first Hopf bifurcation occurs at $Re_2 \approx 4126$ and the second at $Re_3 \approx 4348$. These two thresholds have been calculated by a quadratic interpolation from the amplitudes. The Hopf bifurcations give rise to limit cycles LC_2 and LC_3. LC_2 is stable from its threshold until $Re'_2 \approx 4600$ where it loses stability to LC_3. LC_3 is unstable from Re_3 to $Re'_3 \approx 4410$ and above this Reynolds number it becomes stable. Between LC_2 and LC_3 in the overlap region $Re \in [4400, 4600]$ there exists a quasi-periodic state QP, which has been computed by using $\alpha LC_2 + (1-\alpha)LC_3$ as an initial condition for the full nonlinear simulation where $\alpha = \alpha(Re)$. (*b*) From left to right, the schematic phase portraits corresponding to the bifurcation diagram. The ordinate and abscissa can be considered to be projections onto the eigenmodes leading to LC_2 and LC_3, respectively. The black dots and hollow circles show the stable and unstable states. (i) Stable base flow. (ii) Limit cycle LC_2 is shown as bifurcating in the vertical direction. (iii) LC_3 bifurcates in the horizontal direction. (iv,v) The circle moving on the orbit indicates the quasi-periodic state QP. (vi) QP has disappeared, stabilizing LC_3.

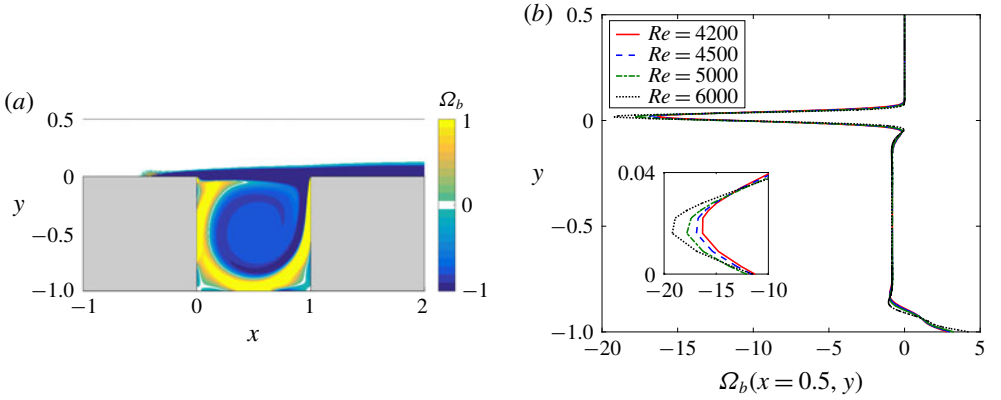

FIGURE 5. (Colour online) Stationary solution (base flow). (*a*) Ω_b over the domain for $Re = 4500$. (*b*) Vorticity profiles $\Omega_b(x = 0.5, y)$ for $Re = 4200, 4500, 5000, 6000$. The major change in the base flow with Reynolds number is localized on the shear layer region and at the bottom of the cavity.

4200 to 6000. These profiles show the increasing steepness of the shear layer at the top of the cavity.

In addition to base flows, we wish to show representations of the limit cycles LC_2 and LC_3. For the flows in our study, the fluctuations are always dominated by the base or mean flow. In figure 6, we show visualizations of the vorticity Ω_2, horizontal velocity u_2 and vertical velocity v_2 for an instantaneous flow from LC_2. Panels (*a–c*) show the full fields and panels (*d–f*) show the fluctuations obtained by subtracting the temporal mean of each field. The temporal means are not shown, since they are visually indistinguishable from the full fields. Although oscillations can be seen in Ω_2 in figure 6(*a*), these are very weak, and even less visible in u_2, v_2 in figure 6(*b*,*c*). Therefore to distinguish between LC_2 and LC_3 and the base flow, we examine the fluctuations, where the periodic structures along the top and downstream side of the cavity are quite visible. Both Ω_2' and u_2' in figure 6(*d*,*e*) display a two-layer structure with an abrupt vertical change of sign at the top of the cavity. Since we are interested primarily in the horizontal variation and propagation of structures along the top of the cavity, we choose to plot the quantity which most emphasizes this feature, namely the vertical velocity fluctuations v_2', as in figure 6(*f*).

In figures 7 and 8 we show the instantaneous vertical velocity fluctuations for LC_2 and LC_3 over one period. LC_2 and LC_3 are also depicted in the supplementary movies available at https://doi.org/10.1017/jfm.2019.422. We observe four structures, i.e. two maxima and two minima of the vertical velocity fluctuations, in LC_2 and six structures, i.e. three maxima and three minima of the vertical velocity fluctuations, in LC_3. Similar visualizations can be seen in calculations by Barbagallo *et al.* (2009) and experiments by Basley *et al.* (2011, 2013).

The behaviour resembles that of travelling waves. The structures, produced by a feedback mechanism, progress steadily to the right but the overall amplitude is not uniform. At the downstream corner, the structures split, as reported by Rockwell & Knisely (1980): one part follows the fluid downstream, while the other is entrained by the cavity recirculation and returns to feed the flow at the upstream corner, sustaining the vortex generation. The mechanism producing the oscillations is the same for both limit cycles LC_2 and LC_3. The temporal frequency is near 7 for LC_2 and near 10

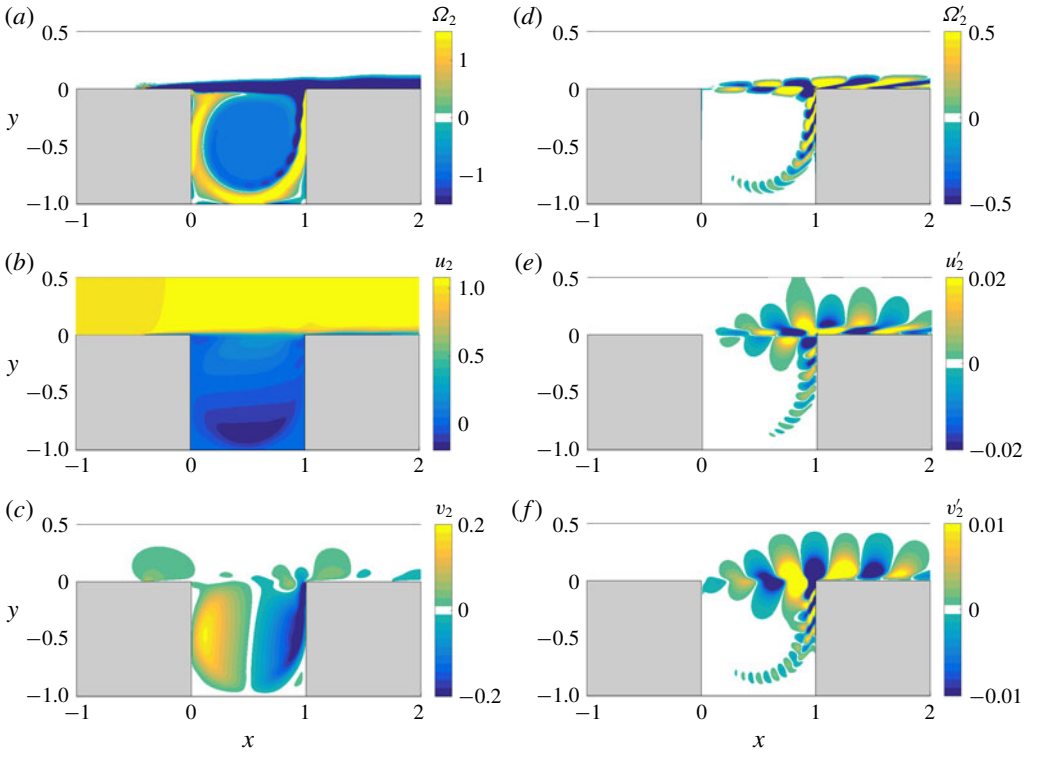

FIGURE 6. (Colour online) Instantaneous visualizations of LC_2 at $Re = 4500$. Panel (*a–c*) shows the spanwise vorticity Ω_2, the horizontal velocity u_2, and the vertical velocity v_2. Panel (*d–f*) shows the fluctuations, obtained by subtracting the mean, e.g. $\Omega_2' = \Omega_2 - \overline{\Omega}_2$, where $\overline{\Omega}_2$ is the average over one temporal period. The mean fields $\overline{\Omega}_2$, $\overline{u}_2$, $\overline{v}_2$ are almost identical to the instantaneous fields and are therefore not shown.

for LC_3, as in Sipp & Lebedev (2007), Meliga (2017). These modes are selected by the cavity length and the mean velocity of the mixing layer as described by Rossiter (1964) and as will be discussed in § 4.4.

3.2. *Linearization about the base flow*

In figure 9 we present the results of linear stability analysis about the base flow. We plot the growth rates σ in figure 9(*a*,*c*) and the frequencies ω in figure 9(*b*,*d*). As previously stated, two successive Hopf bifurcations correspond to two different modes. We plot in (*a*,*b*) the eigenvalue leading to LC_2 and (*c*,*d*) that corresponding to LC_3. The zero crossing of the growth rate marks the Hopf bifurcation at which the base flow becomes unstable to that eigenmode. As presented in the bifurcation diagram in figure 4, the base flow acquires a first unstable direction at around $Re_2 \approx 4126$ and a second unstable direction at $Re_3 \approx 4348$. Figure 9(*b*,*d*) also shows the nonlinear frequencies for the two limit cycles. These agree with the eigenfrequencies at Re_2 and Re_3, as is necessarily the case for a supercritical bifurcation, but as the Reynolds number increases, the frequencies diverge from one another. The frequency extracted at an early stage of a nonlinear simulation initialized by a small perturbation from the base flow will be equal to that given by linear analysis, but the nonlinear interactions

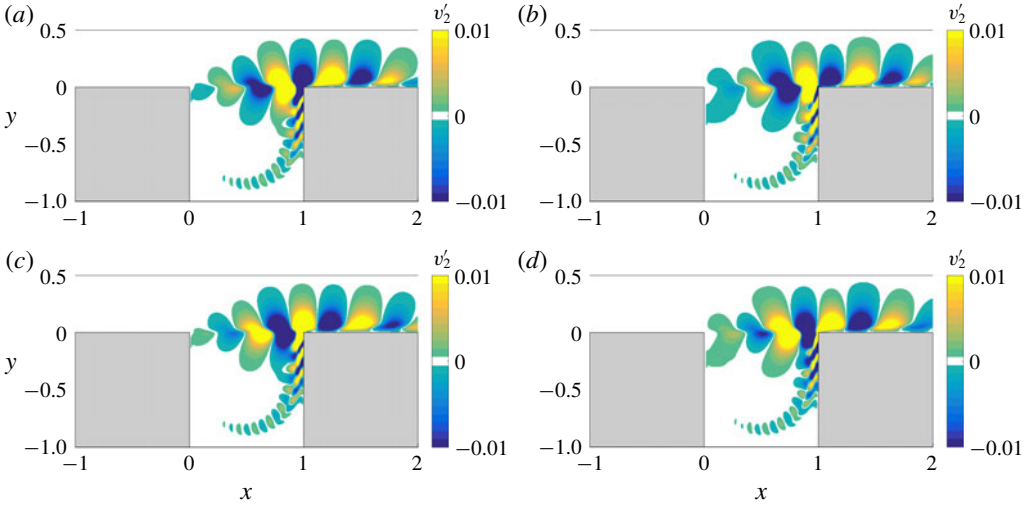

FIGURE 7. (Colour online) Instantaneous vertical velocity fluctuations ($v' = v - \overline{v}$) for LC_2 over one period for $Re = 4500$. (*a*) $t = 0$ (*b*) $T/4$ (*c*) $T/2$ (*d*) $3T/4$. The structures are advected downstream, as they would be for a travelling wave. In the range of the cavity $x \in [0, 1]$ we count two maxima of the vertical velocity fluctuations. The velocity contours are deformed downstream for $x > 1.2$, due to the change to a free-slip boundary condition.

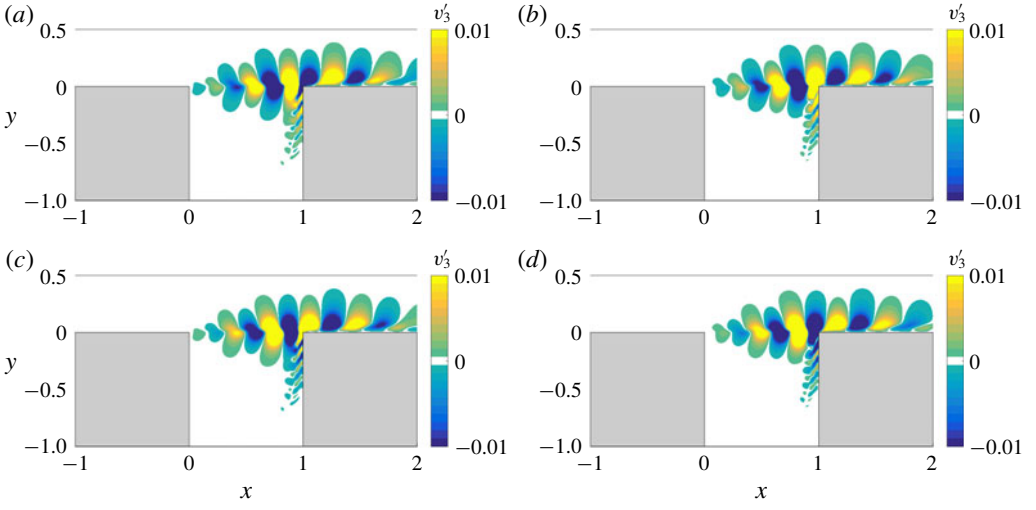

FIGURE 8. (Colour online) Instantaneous vertical velocity fluctuations ($v' = v - \overline{v}$) for LC_3 over one period for $Re = 4500$. (*a*) $t = 0$ (*b*) $T/4$ (*c*) $T/2$ (*d*) $3T/4$. We observe the same dynamics as in LC_2 shown in figure 7. Over the range $x \in [0, 1]$ we count three maxima of the vertical velocity fluctuations.

will cause it to evolve with time to the nonlinear frequency. The frequencies leading to LC_2 and LC_3 cross at $Re = 4540$ (differing by only 0.6 % from the value $Re = 4567$ reported by Meliga (2017)). Below this value of Re, a simulation initialized with a small perturbation from the base flow will converge to LC_2, while above, it will

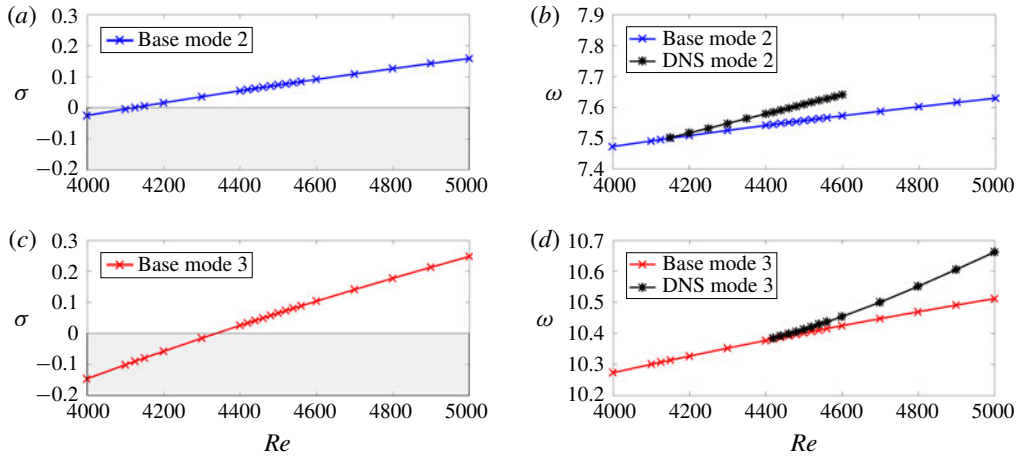

FIGURE 9. (Colour online) Eigenvalues $\sigma + \mathrm{i}\omega$ from linear stability analysis about the base solution with blue and red crosses, and nonlinear frequency from direct numerical simulations (DNS) with black stars. (*a*,*c*) Growth rate σ of the most unstable eigenmode. In this range of Reynolds number, are two successive Hopf bifurcations as shown in the bifurcation diagram of figure 4. The growth rates for eigenvalues leading to LC_2 and LC_3 are shown with blue and red stars respectively. (*b*,*d*) Frequency ω of linear stability analysis about the base state and nonlinear simulation. The nonlinear and linear frequencies agree at onset, but when we increase the Reynolds number the nonlinear frequency deviates from that resulting from linear stability about the base flow.

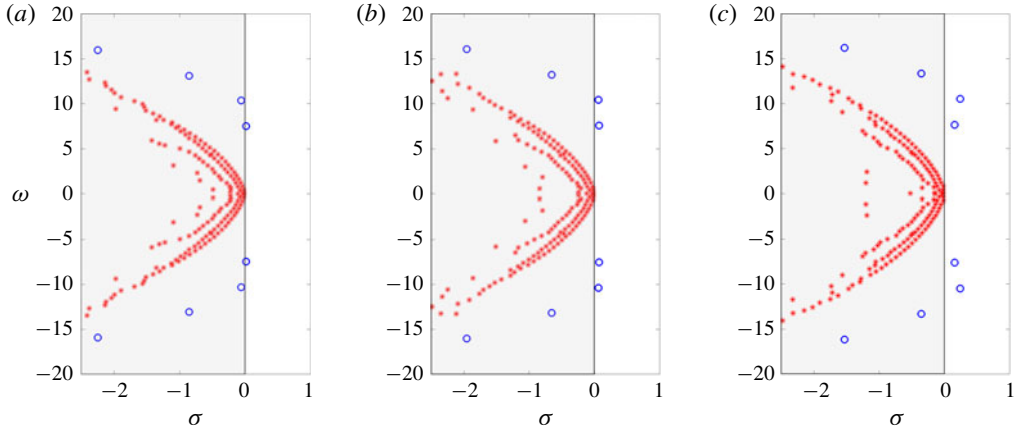

FIGURE 10. (Colour online) Spectra of complex-conjugate eigenvalues of the base flow for (*a*) $Re = 4200$, (*b*) $Re = 4500$, (*c*) $Re = 5000$. Blue circles designate the converged eigenvalues and red stars the eigenvalues that did not converge. In these figures we observe the evolution of modes leading to LC_2 and LC_3. The third converged mode, which is stable in this range of Reynolds number, crosses the imaginary axis for $Re \approx 6000$ (not shown).

converge to LC_3. In contrast, transition from LC_2 to LC_3 will take place when Re is increased above $Re'_2 \approx 4600$ and from LC_3 to LC_2 when Re is decreased below $Re'_3 \approx 4410$.

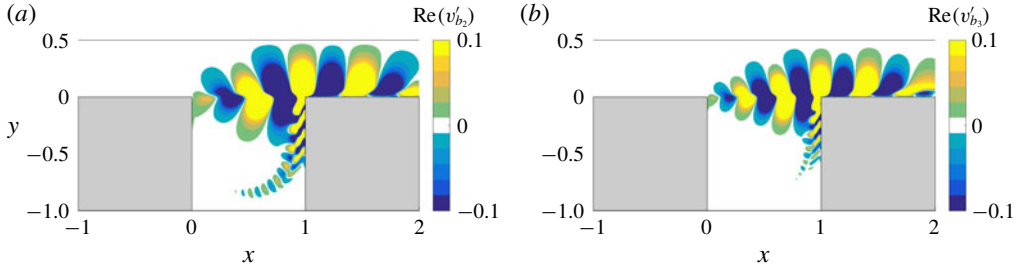

FIGURE 11. (Colour online) Vertical velocity of the real parts of the leading unstable eigenmodes about the base flow at $Re = 4500$. (*a*) LC_2 and (*b*) LC_3.

Figure 10 shows a portion of the eigenvalue spectra for $Re = 4200$, 4500 and 5000. We show in blue circles the eigenvalues that satisfied the convergence tolerance of 10^{-6} and in red stars those that did not converge. The first eigenvalue has crossed the $\sigma = 0$ axis by $Re = 4200$ and the second eigenvalue has crossed by $Re = 4500$. At this Re there are two unstable eigenvalues with almost the same growth rate. At $Re = 5000$ these two unstable eigenvalues have further increased and a third stable mode approaches the imaginary axis, becoming unstable at $Re \approx 6000$ (not shown).

Figure 11(*a*,*b*) shows the real parts of the eigenvectors leading to LC_2 and to LC_3. We observe two vertical velocity fluctuation maxima on LC_2 and three on LC_3, as was mentioned in the discussion of figures 7 and 8.

3.3. *Spatial analysis and Hilbert transform*

We have shown in the previous sections that LC_2 and LC_3 have different numbers of structures across the cavity. Figure 12(*a*,*b*) shows the vorticity fluctuations Ω' slightly above the cavity like those shown in figure 6(*d*), at $y = 0.05$ and for $x \in [0, 2.5]$ for these limit cycles. Curves from light to dark show the vorticity fluctuations at various phases of the temporal period. These two figures show qualitatively the behaviour of a travelling wave, but quantitatively the wavelength and amplitude are not constant. For this reason, at a fixed time, i.e. for each curve shown in figure 12(*a*,*b*), we compute an average wavelength $\overline{\lambda}$. Averaging the wavelength over only $x \in [0, 1]$ is not possible because this range contains too few wavelengths. Figure 12(*c*) shows $\overline{\lambda}$ as the dashed and solid curves for LC_3 and LC_2. The wavelengths vary little over time and have temporal averages $\langle\overline{\lambda_2}\rangle = 0.56$ and $\langle\overline{\lambda_3}\rangle = 0.39$.

We use the Hilbert transform presented in § 2.7 to analyse in detail the final curve $\Omega'(x, y = 0.05)$ shown in figure 12(*a*,*b*). We recall that the Hilbert transform produces from a real signal $f(x)$ a complex signal $f_a(x)$ which is written in polar form as $A(x)e^{i\Phi(x)}$. We show in figure 13(*a*,*b*) the vorticity fluctuations $\Omega'_2(x)$ and $\Omega'_3(x)$ for LC_2 and LC_3 with black curves. Because the Hilbert transform is very sensitive, we have interpolated the signals by cubic splines. The figure also shows the amplitudes $A(x)$ of the Hilbert transform of the signals. Over the range $x \in [0.5, 2.3]$, there are two influential locations: the downstream corner at $x = 1$, and the changeover of boundary condition at $x = 1.75$ from no slip to free slip. The amplitudes $A(x)$ show maxima at the downstream corner. Figure 13(*c*) shows the phase $\Phi(x)$ for LC_2 and LC_3. The slope of $\Phi(t)$ is the wavenumber k. We show with dashed and dotted lines the linear regression calculated over $x \in [0.5, 1.5]$. The wavenumber for LC_2 obtained in this way is $k = 12.115$ and that for LC_3 is $k = 16.045$, leading to wavelengths $\lambda_2 = 0.519$

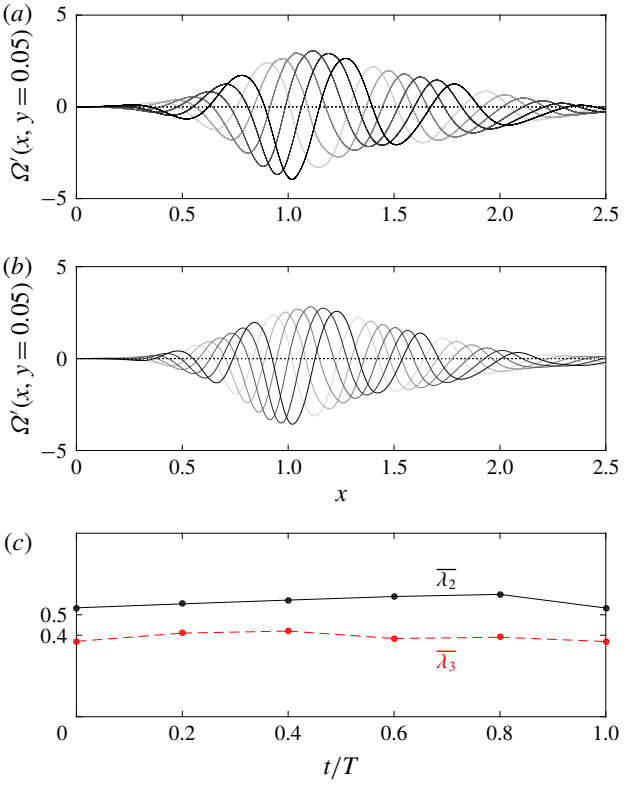

FIGURE 12. (Colour online) Vorticity fluctuations above the cavity $\Omega'(x, y = 0.05)$ over one period. We observe the behaviour of a travelling wave for (*a*) LC_2 and (*b*) LC_3. Because the wavelength evolves in space, we calculate the average wavelength $\overline{\lambda}$ as shown in figure (*c*), in solid and dashed line for LC_2 and LC_3 respectively. The mean wavelength is near 0.5 for LC_2 and near 0.4 for LC_3.

and $\lambda_3 = 0.392$. These values are fairly close to the values $\langle\overline{\lambda}_2\rangle = 0.56$ and $\langle\overline{\lambda}_3\rangle = 0.39$ obtained by measuring wavelengths, as shown in figure 12. The value $\lambda_2 \approx 0.5$ justifies our designation of LC_2 as containing two vertical velocity fluctuation maxima, since $L/\lambda_2 \approx 2$, but the value $\lambda_3 \approx 0.4$ leads to $L/\lambda_3 \approx 2.5$ rather than 3.

3.4. *Quasi-periodic state and Floquet analysis*

As presented in the previous sections, there is a range of Re over which two limit cycles coexist, separated by a quasi-periodic state QP. We mention here that this state is probably periodic rather than strictly quasi-periodic, because of the well-known nonlinear phenomenon of frequency locking, but its effective period is very long and we will continue to consider it to be quasi-periodic. Figures 2 and 3(*b*) show the time series corresponding to this state. Figure 14 presents temporal Fourier spectra for three values of Re. The QP state has two fundamental frequencies close to ω_2 and ω_3 as shown by the dotted and dashed lines in figure 14(*a–c*). QP can be viewed as a nonlinear superposition of LC_2 and LC_3

$$\boldsymbol{U}_{QP}(x, y, t) = \sum_n \sum_m c_{n,m} \mathrm{e}^{\mathrm{i}(n\omega_{QP_2} + m\omega_{QP_3})t}, \tag{3.2}$$

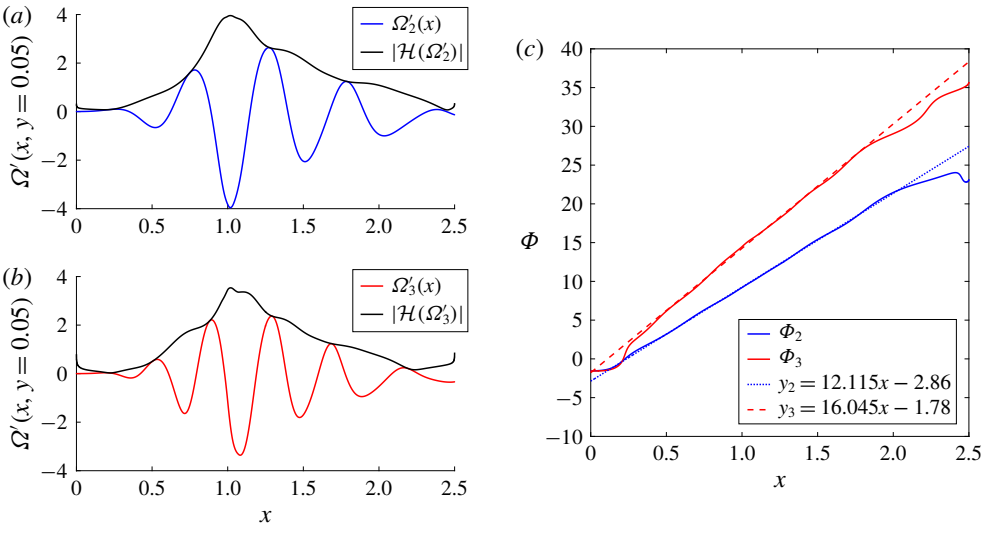

FIGURE 13. (Colour online) Hilbert transform of vorticity fluctuations $\Omega'(x, y = 0.05)$. (*a*,*b*) vorticity fluctuation, its spline interpolation and the modulus of the Hilbert transform, which is the envelope of the signal. (*c*) The ratio between the real and imaginary parts of the Hilbert transform is the phase whose evolution is shown for LC_3 (red) and for LC_2 (blue). Linear fits to the phases Φ_i are shown by dashed and dotted curves.

where $n, m \in \mathbb{N}$, and ω_{QP_2} and ω_{QP_3} are the fundamental frequencies of QP. The blue dotted lines show the nonlinear frequency of LC_2 and the red dashed lines that of LC_3 at the corresponding values of Re.

We now interpret the spectra of figure 14 in the context of the bifurcation diagram of figure 4. Because $Re = 4420$ is close to Re'_3, the quasi-periodic state at $Re = 4420$ is close to the limit cycle LC_3. In agreement with this, the peak at ω_{QP_3} matches almost exactly the nonlinear frequency $\omega_3 = 10.38$ of LC_3 indicated by the red dashed line in figure 14(*a*). In contrast QP is not close to LC_2 at this Reynolds number and so the peak at ω_{QP_2} is to the left of the frequency $\omega_2 = 7.58$ of LC_2 (blue dotted line). At figure 14(*c*), corresponding to $Re = 4580$ near Re'_2, the situation is naturally reversed. The peak at ω_{QP_2} matches almost exactly its analogue $\omega_2 = 7.634$ on LC_2 (blue dotted line) since it is close to LC_2, while ω_{QP_3} is slightly to the right of $\omega_3 = 10.445$ of LC_3. Away from LC_2 and LC_3 at $Re = 4500$, both frequencies $\omega_2 = 7.609$ and $\omega_3 = 10.412$ are slightly shifted from their analogues on the quasi-periodic state.

We have found from the nonlinear simulations that LC_2 loses stability towards LC_3 for $Re > Re'_2 \approx 4600$ and LC_3 gains stability for $Re > Re'_3 \approx 4420$. To shed light on the stability of these limit cycles, we carry out a Floquet analysis. In the Floquet framework, we decompose the velocity field as

$$\boldsymbol{U}(x, y, t) = \boldsymbol{U}_{LC}(x, y, t) + \epsilon \mathrm{e}^{(\sigma_F + \mathrm{i}\omega_F)t} \boldsymbol{u}_F(x, y, t) + \text{c.c.}, \tag{3.3}$$

with $\boldsymbol{U}_{LC}$ the periodic solution corresponding to the limit cycle about which the Floquet analysis is performed, $\boldsymbol{u}_F$ the Floquet mode which is also periodic with period $T_b = 2\pi/\omega_b$ and $\sigma_F + \mathrm{i}\omega_F$ the Floquet exponent. We rewrite (3.3) by expressing the Floquet mode as a Fourier series, leading to

$$\boldsymbol{U}(x, y, t) = \boldsymbol{U}_{LC}(x, y, t) + \epsilon \mathrm{e}^{(\sigma_F + \mathrm{i}\omega_F)t} \sum_n \boldsymbol{u}_{F,n}(x, y) \mathrm{e}^{\mathrm{i}n\omega_b t} + \text{c.c.} \tag{3.4}$$

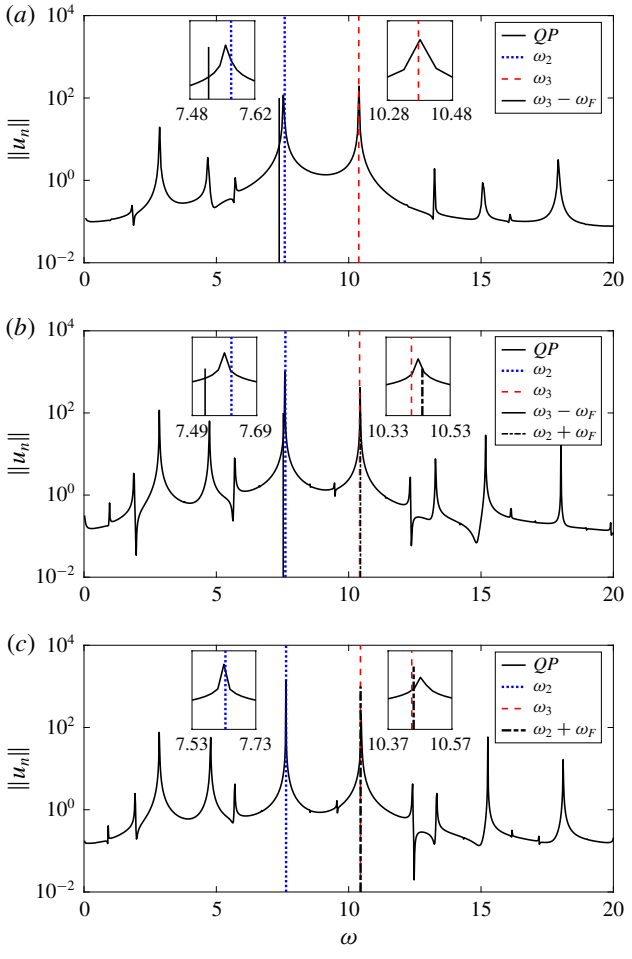

FIGURE 14. (Colour online) Temporal Fourier spectra of the quasi-periodic state (black bold curves), computed with the edge state technique at (*a*) $Re = 4420$, near Re'_3, (*b*) $Re = 4500$ and (*c*) $Re = 4580$, near Re'_2. The vertical lines show the frequencies ω_2 (blue dotted lines) and ω_3 (red dashed lines) of LC_2 and LC_3 at the corresponding values of Re. (*a*) Near Re'_3 where QP is near LC_3, the peak ω_{QP_3} of the QP spectrum matches its analogue ω_3 (red dashed line) on LC_3, while ω_{QP_2} is slightly to the left of ω_2 (blue dotted line) of LC_2. (*c*) Near Re'_2, where QP is near LC_2, the peak of ω_{QP_2} of the QP spectrum matches its analogue ω_2 (blue dotted line), while ω_{QP_3} is to the right of ω_3 (red dashed line) from LC_3. (*b*) Away from Re'_2 and Re'_3, both frequencies ω_{QP_2} and ω_{QP_3} are shifted slightly from their analogues on LC_2 and LC_3. The vertical bold and dash-dotted lines show the frequencies calculated by Floquet analysis about LC_2 by $\omega = \omega_2 + \omega_F$ (dash-dotted line) and about LC_3 by $\omega = \omega_3 - \omega_F$ (bold line). Near the thresholds at (*a*) $Re = 4420$ and (*c*) $Re = 4580$, the frequency obtained by Floquet analysis about LC_3 and LC_2 are very close to ω_{QP_2} and ω_{QP_3}. At $Re = 4500$ in figure (*b*) the frequencies obtained by Floquet analysis about LC_2 and LC_3 are also close to their analogues in the quasi-periodic state even though the linear analysis is only valid at the vicinity of the thresholds.

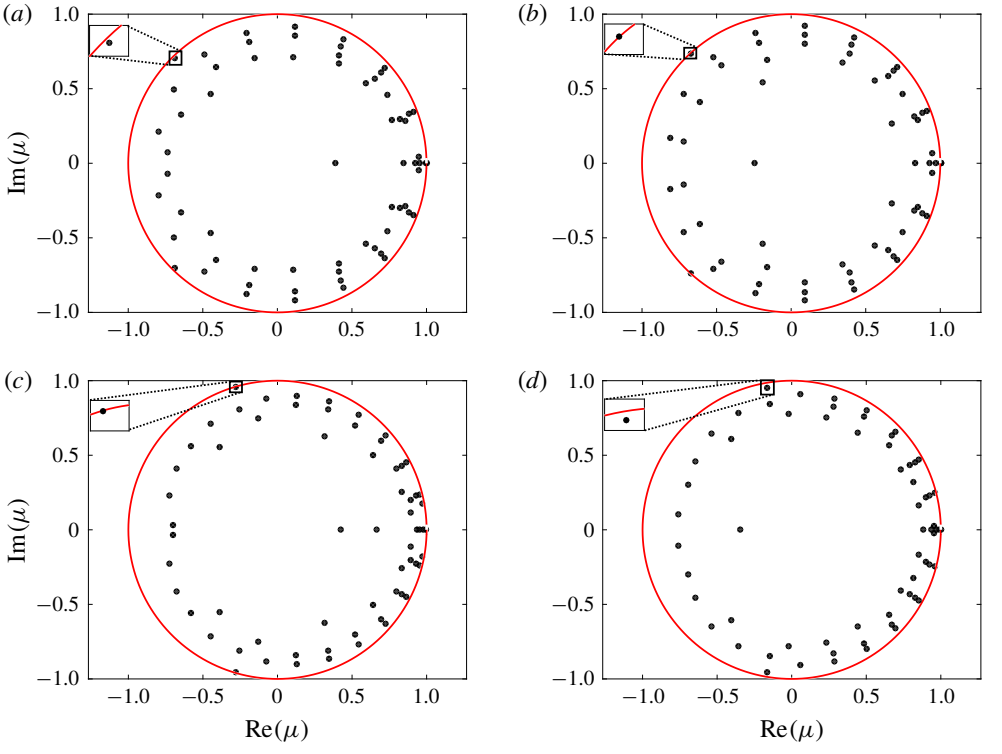

FIGURE 15. (Colour online) Floquet multipliers for LC_2: (*a*) $Re = 4500$, (*b*) $Re = 4600$ and LC_3: (*c*) $Re = 4420$, (*d*) $Re = 4500$. The small boxes are enlargements of the region surrounding the dominant Floquet multiplier.

For $t = T_b$, we have $\mathrm{e}^{\mathrm{i}n\omega_b T_b} = \mathrm{e}^{\mathrm{i}n\omega_b(2\pi/\omega_b)} = \mathrm{e}^{\mathrm{i}n2\pi} = 1$ and so (3.4) becomes

$$\boldsymbol{U}(x, y, T_b) = \boldsymbol{U}_{LC}(x, y, T_b) + \epsilon \mathrm{e}^{\sigma_F 2\pi/\omega_b} \mathrm{e}^{\mathrm{i}2\pi\omega_F/\omega_b} \sum_n \boldsymbol{u}_{F,n}(x, y) + \text{c.c.}, \tag{3.5}$$

with $\mu \equiv \mathrm{e}^{\sigma_F 2\pi/\omega_b}$ the modulus and $\theta \equiv 2\pi\omega_F/\omega_b$ the argument of the Floquet multipliers.

Figure 15 shows the Floquet multipliers for both limit cycles in the complex plane. All Floquet multipliers (dots) are inside the unit circle, meaning that the corresponding limit cycles are stable at these Reynolds numbers. Figure 15(*a*,*b*) shows the results for LC_2 at $Re = 4500$ and 4600 respectively. In figure 15(*a*) at $Re = 4500$, the dominant Floquet multiplier modulus is $|\mu| = 0.981$. On figure 15(*b*), by $Re = 4600 \lesssim Re_2'$, this multiplier has moved closer to the unit circle, with $|\mu| = 0.999$. Figure 15(*c*,*d*) shows that the moduli of the dominant Floquet multipliers for LC_3 at $Re = 4420 \gtrsim Re_3'$ and at $Re = 4500$ are $|\mu| = 0.995$ and $|\mu| = 0.967$. Thus the results shown by the Floquet analysis confirm the nonlinear observations. The results of this Floquet analysis resemble those found for the lid-driven cavity by Tiesinga *et al.* (2002).

We now turn to the argument of the Floquet multipliers. If the Floquet exponent is real ($\omega_F = 0$) then the Floquet multiplier is one and the bifurcating state has the same frequency as the base limit cycle. If $\omega_F/\omega_b = 1/2$ then the Floquet multiplier is -1, which corresponds to a subharmonic mode. In our problem the dominant Floquet

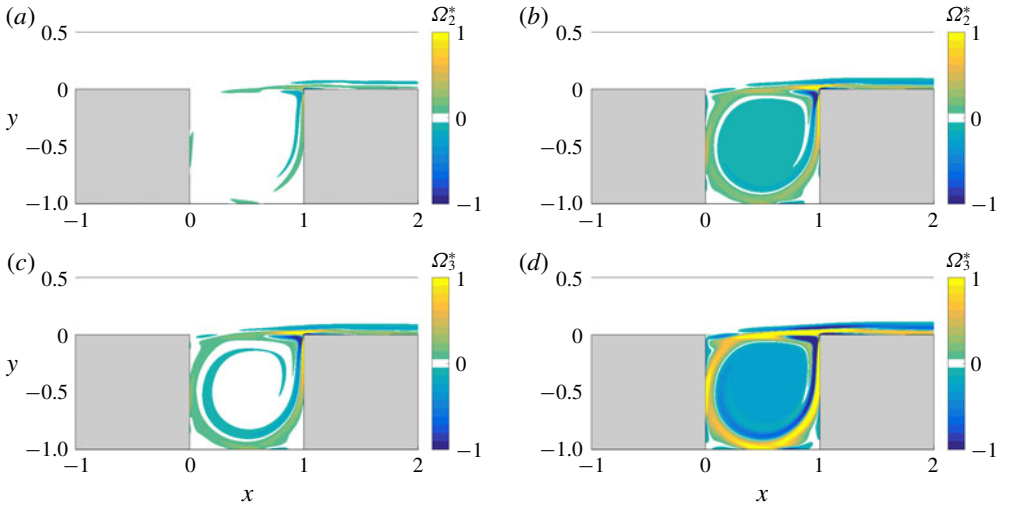

FIGURE 16. (Colour online) Distortion of the mean flow ($\Omega^* = \overline{\Omega} - \Omega_b$). For LC_2 at (*a*) $Re = 4200$ and (*b*) $Re = 4500$. For LC_3 at (*c*) $Re = 4500$ and (*d*) $Re = 5000$. The distortion measures the deviation of the mean flow from the base flow due to nonlinear interaction and increases with Reynolds number.

multiplier is complex, and so the bifurcation is a secondary Hopf bifurcation and the solution near the threshold of QP is described by (3.4). The spectrum of QP near the threshold contains ω_b and its multiples as well as the frequencies introduced by the secondary Hopf bifurcation, namely $\pm\omega_F \pm n\omega_b$, with a dominant contribution from $n = \pm 1$. Indeed, near Re_2', the spectrum of QP contains frequencies ω_2 and $\omega_2 + \omega_F = \omega_2(1 + \theta/2\pi) = 10.45$ while near Re_3', QP contains frequencies ω_3 and $\omega_3 - \omega_F = \omega_3(1 - \theta/2\pi) = 7.37$.

These calculations are confirmed by figure 14(*a*,*c*). For (*a*) $Re = 4420 \gtrsim Re_3'$, the Floquet analysis about LC_3 yields a frequency $\omega_3 - \omega_F$ (solid vertical black line) comparable to the peak at ω_{QP_2} For (*c*) $Re = 4580 \lesssim Re_2'$, the Floquet analysis about LC_2 yields the frequency $\omega_2 + \omega_F$ (dashed vertical black line) which is very close to ω_{QP_3}.

4. Frequency prediction

4.1. *Linearization about the mean flow*

Linear stability analysis – i.e. linearizing about the base flow and solving the resulting eigenproblem – is a classic tool in hydrodynamics. Bifurcations which create new branches are determined unambiguously by linear stability analysis and, if the bifurcation is supercritical, the spatial and temporal behaviours of the new states near threshold are similar to those of the eigenvector and eigenvalue responsible for the instability. Further from the threshold, these properties evolve and may well differ substantially from those of the bifurcating eigenvector and eigenvalue. In some cases, it has been shown that linearization about the mean flow of a limit cycle can yield more accurate approximations of the nonlinear states. We have carried out a linear analysis about the temporal mean for both limit cycles LC_2 and LC_3 and compared the resulting frequencies with those obtained from linearization about the base flow

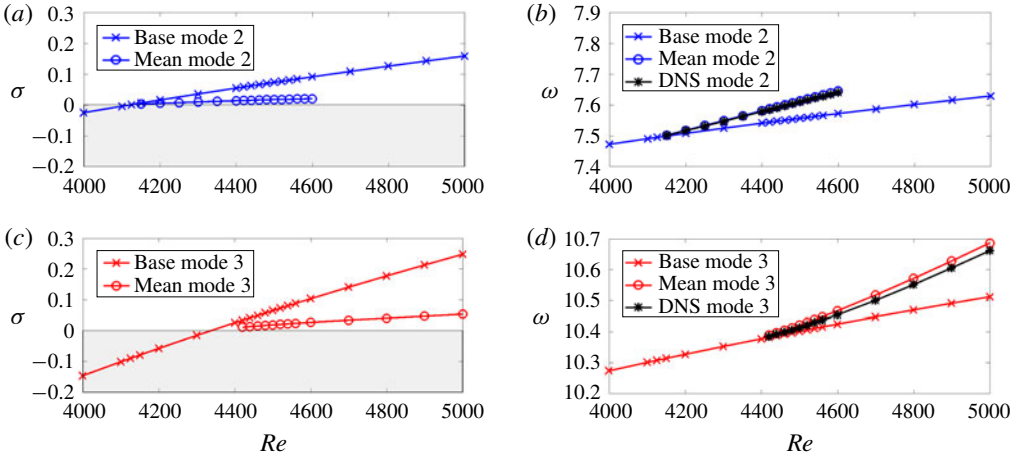

FIGURE 17. (Colour online) Eigenvalues $\sigma + \mathrm{i}\omega$ from linear stability analysis about the base and mean flows of LC_2 and LC_3. The eigenvalues about the base flow are plotted with crosses. Linear stability about the mean flow is shown with circles. The nonlinear frequency from DNS is plotted with black stars. (*a*,*c*) The growth rate σ for LC_2 for the mean flow is nearly zero but that of LC_3 is smaller than that about the base flow, but not enough to be considered to be neutrally stable. (*b*,*d*) The imaginary parts of the eigenvalues are almost exactly equal to the nonlinear frequencies, especially for LC_2. For LC_3, although the imaginary part of the eigenvalue and the nonlinear frequency are necessarily equal at onset, the two diverge slightly as Re increases.

and with the nonlinear frequencies of these cycles. This procedure has been carried out for LC_3 by Meliga (2017); here we carry out the same procedure for LC_2 and compare the two regimes.

The mean flow greatly resembles the base flow shown in figure 5, and therefore we plot instead their difference, the distortion $\overline{\Omega}^* \equiv \overline{\Omega} - \Omega_b$, which is shown for LC_2 at $Re = 4200$ and 4500 in figure 16(*a*,*b*) and for LC_3 at $Re = 4500$ and 5000 in figure 16(*c*,*d*). Nor do we show the eigenmodes obtained by linearizing about the mean flow, since they resemble those obtained from linearizing about the base flow (figure 11) as well as the nonlinear vertical velocity fluctuations (figures 7 and 8).

Figure 17 and table 1 compare the eigenvalues resulting from linearization about the base flow and the mean flow and those of the nonlinear simulation. Figure 17 plots the frequencies and growth rates over the Reynolds number range [4000, 5000] that we have studied, while table 1 shows numerical data extracted from these figures for three representative Reynolds numbers, 4200, 4500 and 5000. We note that unlike for the cylinder wake (Barkley 2006), the frequencies obtained from the usual linear stability analysis are already not very far from those of the nonlinear limit cycles. Table 1 shows a deviation of less than 0.6 % for the frequencies in LC_2 and of less than 1.4 % for LC_3 over this Reynolds number range. In contrast, for the cylinder wake (Barkley 2006), the difference between the nonlinear frequencies and those obtained by linear stability analysis reaches 15 % by $Re = 60$, a Reynolds number comparable to the distance above criticality studied here and reaches 100 % by $Re = 180$, a frequent upper limit of such studies. This difference will be discussed further in §§ 4.4 and 5.

Figure 17(*b*) for LC_2 (circles) shows that the frequency obtained by linearization about the mean flow is nonetheless much closer to the nonlinear temporal frequency

	Linearize about base			Linearize about mean			Nonlinear			$\Delta\omega$	Δf
Re	4200	4500	5000	4200	4500	5000	4200	4500	5000	—	—
ω_2	7.502	7.556	7.629	7.517	7.612	—	7.516	7.609	—	2.8	0.45
diff	0.014	0.053	—	0.001	0.003	—	—	—	—	—	—
σ_2	0.016	0.073	0.158	0.005	0.017	—	—	—	—	—	—
ω_3	10.327	10.401	10.512	—	10.421	10.686	—	10.412	10.661	2.8	0.45
diff	—	0.011	0.149	—	0.009	0.025	—	—	—	—	—
σ_3	−0.058	0.065	0.247	—	0.018	0.053	—	—	—	—	—
ω_4	13.099	13.188	13.321	—	—	—	—	—	—	2.8	0.45
ω_5	15.931	16.029	16.183	—	—	—	—	—	—	—	—

TABLE 1. Linear and nonlinear frequencies for cavity modes. The first row shows frequencies from linearization about the base and from linearization about the mean and nonlinear simulations, where available. Second row for ω_2 and ω_3 shows deviation from frequencies from nonlinear simulations. When the RZIF property is satisfied, linearization about the nonlinear mean yields frequencies close to nonlinear frequencies. The third row for ω_2 and ω_3 shows linear growth rates for cavity modes. Linearization about the base flow yields growth rates which cross zero transversely as the bifurcation threshold is crossed. When the RZIF property is satisfied, linearization about the nonlinear mean yields growth rates near zero, i.e. the mean flow is nearly marginally stable. Last columns show the frequency increment between consecutive eigenvalues, which is constant to two digits, regardless of the Reynolds number or which type of frequency is used.

(stars) than that given by linear stability about the base flow (crosses). Quantitatively, table 1 shows the relative difference at $Re = 4500$ between the nonlinear frequency and the frequency obtained from the base flow to be 0.7 %; this difference is reduced to 0.04 % when the linearization is performed about the mean flow. Moreover, the growth rate obtained about the mean flow (circles) in figure 17(*a*) is nearly zero, as found by Barkley (2006) for the cylinder wake. Table 1 shows a growth rate at $Re = 4500$ of 0.073 for linearization about the base flow; this is reduced by a factor of 5 to 0.017 for the linearization about the mean.

For LC_3, the frequency obtained by linearizing about the mean presented in figure 17(*d*) (circles) agrees well with the nonlinear frequency (stars). The curves begin to diverge slightly for $Re \geqslant 4600$, and although the agreement is not as good as it is for LC_2, the frequencies are still very close. Quantitatively, table 1 shows the relative difference at $Re = 5000$ between the nonlinear frequency and the frequency obtained from the base flow to be 1.4 %; this difference is reduced to 0.02 % when the linearization is performed about the mean flow. Table 1 shows a growth rate at $Re = 5000$ of 0.247 for linearization about the base flow; this is again reduced by a factor of 5 to 0.053 for the linearization about the mean.

4.2. *RZIF and SCM*

We now present an argument for the validity of linearization about the mean flow. The derivation is closely related to the idea called harmonic balance in the aerodynamic literature (Hall, Thomas & Clark 2002; McMullen, Jameson & Alonso 2006; McMullen & Jameson 2006). Turton *et al.* (2015) argued that the RZIF property holds exactly if the time dependence is monochromatic, meaning that

higher harmonics are negligible compared to the fundamental frequency. Consider the evolution equation

$$\partial_t \boldsymbol{U} = \mathcal{L}\boldsymbol{U} + \mathcal{N}(\boldsymbol{U}, \boldsymbol{U}), \tag{4.1}$$

where $\mathcal{L}$ is linear and $\mathcal{N}(\cdot,\cdot)$ is a quadratic nonlinearity. Let

$$\boldsymbol{U} = \overline{\boldsymbol{U}} + \sum_{n\neq 0} \boldsymbol{u}_n \mathrm{e}^{\mathrm{i}n\omega t}, \tag{4.2}$$

(with $\boldsymbol{u}_{-n} = \boldsymbol{u}_n^*$) be the temporal Fourier decomposition of a periodic solution to (4.1) with mean $\overline{\boldsymbol{U}}$ and frequency ω. In (4.2) and throughout this subsection, subscripts refer to temporal harmonics of a single limit cycle, rather than serving to distinguish between LC_2 and LC_3.

The $n=0$ (mean) component of (4.1) is

$$0 = \mathcal{L}\overline{\boldsymbol{U}} + \mathcal{N}(\boldsymbol{u}_1, \boldsymbol{u}_{-1}) + \mathcal{N}(\boldsymbol{u}_{-1}, \boldsymbol{u}_1) + \mathcal{N}(\boldsymbol{u}_2, \boldsymbol{u}_{-2}) + \mathcal{N}(\boldsymbol{u}_{-2}, \boldsymbol{u}_2) + \cdots \tag{4.3}$$

while the $n=1$ component is

$$\begin{aligned} \mathrm{i}\omega \boldsymbol{u}_1 \;=\; & \underbrace{\mathcal{L}\boldsymbol{u}_1 + \mathcal{N}(\overline{\boldsymbol{U}}, \boldsymbol{u}_1) + \mathcal{N}(\boldsymbol{u}_1, \overline{\boldsymbol{U}})}_{\mathcal{L}_{\overline{U}}\boldsymbol{u}_1} \\ & + \underbrace{\mathcal{N}(\boldsymbol{u}_2, \boldsymbol{u}_{-1}) + \mathcal{N}(\boldsymbol{u}_{-1}, \boldsymbol{u}_2) + \mathcal{N}(\boldsymbol{u}_3, \boldsymbol{u}_{-2}) + \mathcal{N}(\boldsymbol{u}_{-2}, \boldsymbol{u}_3) + \cdots}_{\mathcal{N}_1}. \end{aligned} \tag{4.4}$$

If, as is often the case, $\|u_n\| \sim \epsilon^{|n|}$, then $\mathcal{N}_1 = O(\epsilon^3)$ may be neglected and RZIF is satisfied: the linear operator $\mathcal{L}_{\overline{U}}$ in (4.4) has the pure imaginary eigenvalue $\mathrm{i}\omega$, corresponding to the frequency of the periodic solution. Hence the RZIF property is satisfied for near-monochromatic oscillations in a system with quadratic nonlinearity.

We mention here that RZIF is not predictive, since it requires a full nonlinear direct numerical simulation to be carried out in order to compute the temporal mean $\overline{U}$. An approach which is actually predictive, i.e. which does not require a DNS, has been proposed by Mantič-Lugo *et al.* (2014, 2015), who called it the self-consistent model (SCM). The SCM truncates the mean flow equation (4.3) as well as the $n=1$ equation (4.4), leading to the closed system

$$\left.\begin{aligned} 0 &= \mathcal{L}\overline{\boldsymbol{U}} + \mathcal{N}(\boldsymbol{u}_1, \boldsymbol{u}_{-1}) + \mathcal{N}(\boldsymbol{u}_{-1}, \boldsymbol{u}_1), \\ \mathrm{i}\omega \boldsymbol{u}_1 &= \mathcal{L}\boldsymbol{u}_1 + \mathcal{N}(\overline{\boldsymbol{U}}, \boldsymbol{u}_1) + \mathcal{N}(\boldsymbol{u}_1, \overline{\boldsymbol{U}}). \end{aligned}\right\} \tag{4.5}$$

This system is then solved for $\overline{\boldsymbol{U}}$ and $\boldsymbol{u}_1$ by various iterative methods; see Mantič-Lugo *et al.* (2014, 2015). The next higher truncation, i.e. retaining $\overline{\boldsymbol{U}}$, $\boldsymbol{u}_1$, and $\boldsymbol{u}_2$, has been studied by Meliga (2017). It may happen, however, that RZIF is satisfied, while SCM is not, i.e. that while higher-order modes may be neglected in (4.4), they are essential to forming the correct mean flow and cannot be neglected in (4.3); see Bengana (2019).

For thermosolutal convection, Turton *et al.* (2015) showed that for travelling waves, the RZIF property is satisfied and the spectrum is highly peaked, while for standing waves the spectrum is broad and the RZIF property is not satisfied. We now wish to see if the temporal spectra of LC_2 and LC_3 also explain the fact that the RZIF

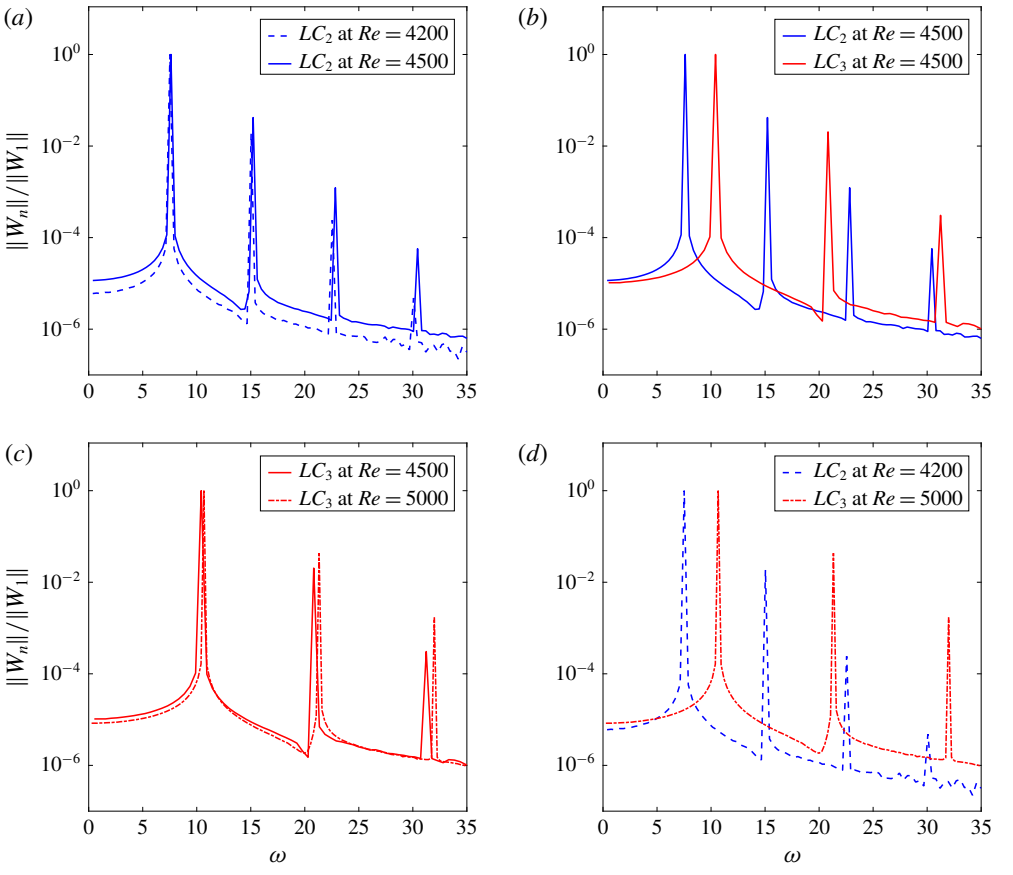

FIGURE 18. (Colour online) Temporal spectra of streamwise velocity normalized by the fundamental frequency for LC_2 and LC_3. (*a*) Spectra of LC_2 at $Re = 4200$ and $Re = 4500$. (*b*) At $Re = 4500$ for LC_2 and LC_3. (*c*) At $Re = 4500$ and $Re = 5000$ for LC_3. (*d*) Spectra of LC_2 and LC_3 at $Re = 4200$ and $Re = 5000$, respectively.

property is better satisfied for LC_2 than for LC_3. We show in figure 18 the temporal spectra of streamwise velocity normalized by the fundamental frequency for LC_2 and LC_3, for various values of Reynolds number. In figure 19 we plot the ratio of the second harmonic to the fundamental frequency. The ratio $\|\hat{u}_2\|/\|\hat{u}_1\|$ is consistently less than 0.05 for both flows over the range of our investigation, while $(\|\hat{u}_2\| + \|\hat{u}_3\| + \|\hat{u}_4\|)/\|\hat{u}_1\|$ remains below 0.07, consistent with the fact that RZIF is satisfied. We observed that RZIF is closer to being valid for LC_2 than for LC_3, but the ratios in figure 19 follow the opposite tendency. Thus, the explanation proposed by Turton *et al.* (2015) in terms of the temporal Fourier amplitudes does not explain this difference.

4.3. *Cross-eigenvalues*

Like the base flow, the mean flow has a full spectrum of eigenvalues and eigenvectors. Thus, the mean flow of LC_2 has not only eigenvectors with two vertical velocity fluctuation maxima with corresponding eigenvalues shown in figure 17(*a*,*b*), like those which lead to LC_2, but it also has also eigenvectors with three maxima like those which lead to LC_3 and their corresponding eigenvalues. Similarly, the mean flow of

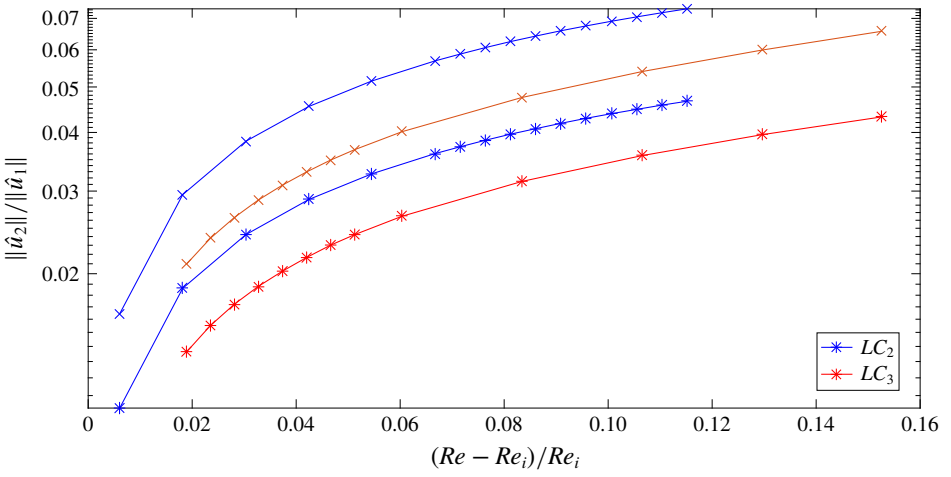

FIGURE 19. (Colour online) Amplitude of second harmonic (stars) and the sum of the amplitudes of the three lowest harmonics (crosses) normalized by the amplitude of the fundamental frequency as a function of relative Reynolds number for LC_2 and LC_3. As in figure 18, the fundamental frequency dominates the second harmonic. These ratios are always below 10^{-1} and are slightly higher for LC_2 than that for LC_3.

LC_3 has eigenvectors containing two maxima. We refer to these as cross-eigenvalues. Figure 20 shows the cross-eigenvalues corresponding to mode two, obtained by linearization about the mean flow of LC_3 (circles, figure 20(*a*,*b*)) and those of mode three about the mean flow of LC_2 (circles, figure 20(*c*,*d*)). The eigenvalues obtained from the base and from the mean necessarily agree at Re_2 for LC_2 and at Re_3 for LC_3, since when the limit cycles are created, the base and mean flows are equal.

Focusing on figure 20(*a*), we recall that LC_3 is created at $Re_3 \approx 4348$ and is unstable to eigenmodes of type 2 until $Re_3' \approx 4410$, i.e. there is a Floquet mode with positive Floquet exponent for $Re \in [4348, 4410]$. This is qualitatively the behaviour that is seen in figure 20(*a*), although here the cross-eigenvalue σ is positive over a higher range, for $Re \in [4348, 4681]$. Focusing now on figure 20(*c*), we recall that LC_2 is created at $Re_2 \approx 4126$ and becomes unstable to eigenmodes of type 3 at $Re_2' \approx 4600$. This is again qualitatively close to the behaviour is seen in figure 20(*c*), except that here the cross-eigenvalue σ becomes positive at the lower value of $Re \approx 4418$.

These results indicate that for a limit cycle, linearization about its mean flow may be able to convey information about the growth rate, frequency, and spatial characteristics of its stability to secondary bifurcations. Referring back to figure 4(*b*), these phase portraits represent the limit cycles as fixed points, whose existence and stability are governed by the dynamics of the two-dimensional normal form (3.1*a*), (3.1*b*). Stability or instability of LC_2 to LC_3 or *vice versa* is represented by the horizonal arrows emanating to or from LC_2, located on the vertical axis, and the vertical arrows emanating to or from LC_3, located on the horizontal axis. The temporal mean would then be interpreted as a fixed point approximation to a limit cycle, and the cross-eigenvalues would then correspond to their relative stability. Although this is plausible, we emphasize that there exists at present no mathematical framework for this interpretation. Moreover, although the trends seen in figure 20 support this interpretation, the agreement is only qualitative.

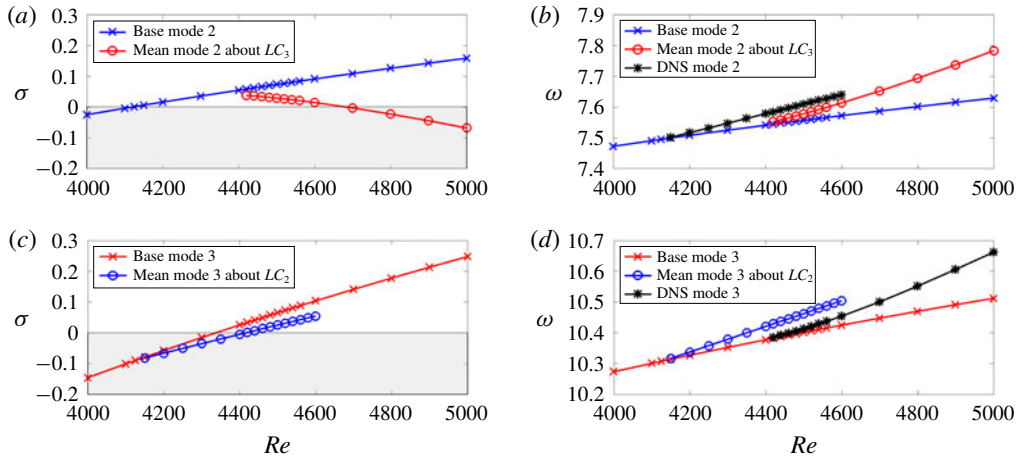

FIGURE 20. (Colour online) Eigenvalues $\sigma + \mathrm{i}\omega$ from linearization about the base and mean flows. Here the spatial form of the eigenvector does not correspond to that of the mean flow. The eigenvalues about the base flow are plotted with crosses, blue for LC_2 and red for LC_3. The eigenvalues of mode two about the mean flow of LC_3 are shown with red circles and that of mode three about the mean flow of LC_2 with blue circles. The nonlinear frequencies from DNS are plotted with black stars for LC_2 and LC_3. (*a*) The growth rate of mode two about the mean of LC_3 (red circles) decreases from the threshold $Re_3 \approx 4348$ of LC_3 and becomes negative at $Re \approx 4681$. This may correspond qualitatively to the fact that LC_3 is unstable to mode 2 perturbations when it is created at Re_3 and becomes stable at $Re_3' \approx 4410$. (*c*) The growth rate of mode three about the mean of LC_2 (blue circles) increases from the threshold $Re_2 \approx 4126$ of LC_2 and becomes positive at $Re \approx 4418$. This may correspond qualitatively to the fact that LC_2 is stable when created at Re_2 and becomes unstable at $Re_2' \approx 4600$.

4.4. *Rossiter formula*

We return to table 1, the last column of which shows that the frequencies of successive modes increase by a constant interval. (For a given mode, the various versions of its frequency differ by at most 1–2 %.) We emphasize this again by reproducing the eigenspectra in figure 21, adding horizontal lines which emphasize visually the constant difference between the frequencies. Spectra similar to those in figure 21 are also seen for the lid-driven cavity in Tiesinga *et al.* (2002).

In flows over shear-driven cavities, Rossiter (1964) observed that the temporal frequencies for self-sustained oscillations were quantized and proposed the following empirical formula:

$$f_n = \frac{U_\infty}{L}\frac{n-\gamma}{M+1/\kappa} \quad \Longrightarrow \quad \frac{U_\infty}{L}\kappa\,(n-\gamma) \quad \text{for } M=0, \tag{4.6}$$

where U_∞ and L are the free-stream speed away from the cavity and the length of the cavity, and M is the Mach number, here set to zero. The phenomenological constant γ is a phase lag, while the increment κ will be discussed below. The essence of (4.6) is not only that the temporal frequencies f_n observed are quantized (which is to be expected in a finite cavity) but that they are separated by a fixed increment Δf. Heuristically, if the limit cycle consists of n structures advected horizontally at velocity U_{adv}, then the average structure occupies a length L/n and strikes the cavity corner

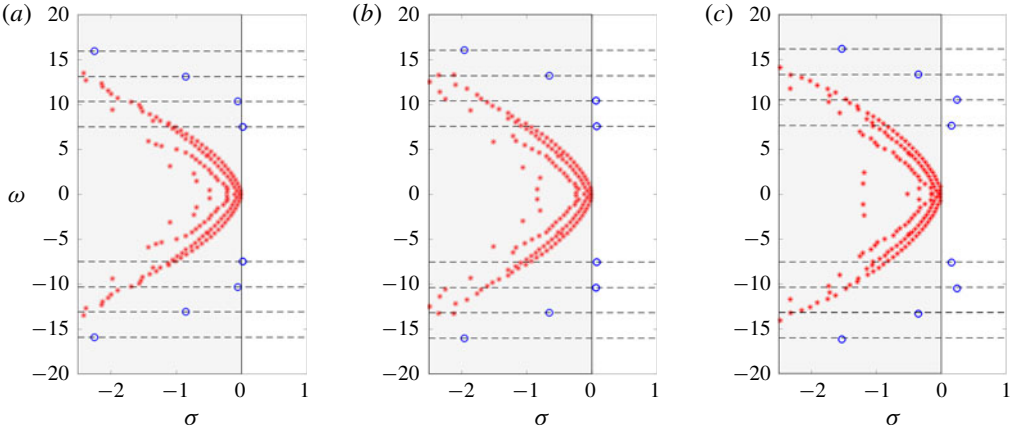

FIGURE 21. (Colour online) Spectra of the base flow for (*a*) $Re = 4200$, (*b*) $Re = 4500$, (*c*) $Re = 5000$. Blue circles designate the converged eigenvalues and red stars the eigenvalues that did not converge. Horizontal lines emphasize the fact that the frequencies are equally spaced.

with frequency $U_{adv}/(L/n)$. Since the frequencies in table 1 are non-dimensionalized by U_∞/L, we have

$$\Delta f = \frac{U_\infty}{L}\kappa = \frac{U_{adv}}{L} = 0.45 \quad \Longrightarrow \quad \kappa = \frac{U_{adv}}{U_\infty} = 0.45. \tag{4.7}$$

Thus, the frequency is seen to be determined primarily by the geometry and the free-stream velocity.

At the same time as Rossiter, Kulikovskii (1966) proposed an approach, involving amplification of the perturbations along the pathway around the cavity, for determining the set of discrete frequencies that appear in a finite domain. Tuerke *et al.* (2015) applied this approach to the open cavity in the incompressible regime and showed very good agreement with the experimental results of Basley *et al.* (2011).

5. Conclusion

We have carried out a detailed study of the dynamics of shear-driven square cavity flow over the Reynolds number range 4000–5000. An original result of the study is the detailed description of two solution branches, which are limit cycles with different numbers of structures, i.e. vertical velocity fluctuation extrema, across the cavity. These appear via successive primary supercritical Hopf bifurcations. Stability is transferred from the first to the second limit cycle via an unstable quasi-periodic state which is created and destroyed via subcritical secondary Hopf bifurcations from the limit cycles. The primary and secondary Reynolds numbers are such that there exists a region of bistability. Transition from one limit cycle to the other is hysteretic and is characterized by a sudden change in frequency from $\omega \sim 7$ to $\omega \sim 10$ and a change in the number of structures along the shear layer of the cavity. By using edge state tracking, we have been able to produce an approximation to the quasi-periodic state and to measure its temporal Fourier spectrum, which corresponds well to the frequencies computed by a Floquet analysis of the two limit cycles. The Hilbert transform is used to extract spatial envelopes and wavenumbers for representatives of these limit cycles.

A possible extension of our study is to the range $Re > 5000$. Although the next two eigenvalue pairs seen in figure 21 cross the imaginary axis, time-dependent simulations do not exhibit these frequencies, as has also been observed by Tiesinga *et al.* (2002) for the lid-driven cavity. Preliminary simulations also show that limit cycle LC_3 may undergo a secondary Hopf bifurcation between $Re = 6000$ and $Re = 7500$. At these Reynolds numbers, the temporal Fourier spectrum shows low-frequency components whose associated spatial characteristics are localized inside the cavity.

Our second focus has been to apply the technique of linearization about the temporal mean of the limit cycles, an approach which has been shown to sometimes describe nonlinear properties. More specifically, in many cases the real part of the leading eigenvalue is near zero (a property which would be described as marginal stability in the context of linearization about the base) and the imaginary part is near the nonlinear frequency of the limit cycles. The combination of these properties is called RZIF.

Based on this study and preceding ones, we can classify hydrodynamic configurations into three categories with respect to the RZIF property. The first is those for which the nonlinear frequencies deviate substantially from those resulting from linearization about the base flow, but are close to those resulting from linearization about the mean flow, and for which the mean flow growth rate is also very small. This category includes the cylinder wake (Barkley 2006; Mittal 2008; Mantič-Lugo *et al.* 2014), for which RZIF has been studied most extensively, as well as the travelling waves of thermosolutal convection (Turton *et al.* 2015), and the ribbons and spirals of counter-rotating Taylor–Couette flow (Bengana & Tuckerman 2019). In the second category, the nonlinear, base flow and mean flow frequencies are all different and the mean flow growth rate is not small, such as the standing waves of thermosolutal convection (Turton *et al.* 2015). In the third category, the difference between the nonlinear and the base flow frequencies and the base flow growth rate is already fairly low. This is what we find for the shear-driven cavity flow at the parameter values we have studied. The frequencies are primarily set by the geometry and the convection velocity. The nonlinear self-sustained mechanism distorts the base flow only slightly, leaving the convection velocity and hence the frequency almost unchanged. Linearization about the mean flow further and substantially reduces these already small differences. It would useful to know *a priori* into which category a hydrodynamic configuration falls. Explanations in terms of travelling or standing waves (Turton *et al.* 2015; Bengana & Tuckerman 2019) have not yet proved satisfactory or complete.

Because the shear-driven cavity flow in our Reynolds number range has two limit cycles, we can take the further step of analysing other eigenmodes of the mean, which do not correspond to the limit cycle. We find that these eigenmodes mimic qualitatively the behaviour of the limit cycles with respect to one other: as the Reynolds number is increased, the real part of one eigenvalue decreases from positive to negative for a limit cycle which undergoes stabilization via a secondary bifurcation, and increases from negative to positive for a cycle which undergoes destabilization. Further investigation, in the form of simulations of other hydrodynamic configurations, and more theoretical understanding, would be necessary to verify whether and when this is a systematic tendency. Another possible direction would be to generalize this type of analysis to quasi-periodic regimes, linearizing about the full temporal mean or else about some other quantity.

In summary, the existence of two competing limit cycles for shear-driven cavity flow has yielded both an interesting bifurcation diagram, containing features such

as subcritical bifurcations, hysteresis and a quasi-periodic state. At the same time, the existence of two cycles has also extended the application and interpretation of linearization about the mean flow.

Acknowledgements

This work was performed using high performance computing resources provided by the Institut du Developpement et des Ressources en Informatique Scientifique (IDRIS) of the Centre National de la Recherche Scientifique (CNRS), coordinated by GENCI (Grand Équipement National de Calcul Intensif), grant nos A0032A06362 and A0042A01119.

Supplementary movies

Supplementary movies are available at https://doi.org/10.1017/jfm.2019.422.

REFERENCES

AIDUN, C. K., TRIANTAFILLOPOULOS, N. G. & BENSON, J. D. 1991 Global stability of a lid-driven cavity with throughflow: flow visualization studies. *Phys. Fluids* A **3** (9), 2081–2091.

ÅKERVIK, E., BRANDT, L., HENNINGSON, D. S., HŒPFFNER, J., MARXEN, O. & SCHLATTER, P. 2006 Steady solutions of the Navier–Stokes equations by selective frequency damping. *Phys. Fluids* **18** (6), 068102.

BARBAGALLO, A., SIPP, D. & SCHMID, P. J. 2009 Closed-loop control of an open cavity flow using reduced-order models. *J. Fluid Mech.* **641**, 1–50.

BARKLEY, D. 2006 Linear analysis of the cylinder wake mean flow. *Europhys. Lett.* **75** (5), 750–756.

BARKLEY, D. & HENDERSON, R. D. 1996 Three-dimensional Floquet stability analysis of the wake of a circular cylinder. *J. Fluid Mech.* **322**, 215–241.

BASLEY, J., PASTUR, L. R., LUSSEYRAN, F., FAURE, T. M. & DELPRAT, N. 2011 Experimental investigation of global structures in an incompressible cavity flow using time-resolved PIV. *Exp. Fluids* **50** (4), 905–918.

BASLEY, J., PASTUR, L. R., DELPRAT, N. & LUSSEYRAN, F. 2013 Space–time aspects of a three-dimensional multi-modulated open cavity flow. *Phys. Fluids* **25**, 064105.

BENEDDINE, S., SIPP, D., ARNAULT, A., DANDOIS, J. & LESSHAFFT, L. 2016 Conditions for validity of mean flow stability analysis. *J. Fluid Mech.* **798**, 485–504.

BENGANA, Y. 2019. Numerical simulations for frequency prediction via mean flows. PhD thesis, PSL Research University. Available at: https://hal.archives-ouvertes.fr/tel-02170483.

BENGANA, Y. & TUCKERMAN, L. S. 2019 Spirals and ribbons in counter-rotating Taylor–Couette flow: frequencies from mean flows and heteroclinic orbits. *Phys. Rev. Fluids* **4**, 044402.

CHIEN, W-L., RISING, H. & OTTINO, J. M. 1986 Laminar mixing and chaotic mixing in several cavity flows. *J. Fluid Mech.* **170**, 355–377.

CUNHA, G., PASSAGGIA, P-Y. & LAZAREFF, M. 2015 Optimization of the selective frequency damping parameters using model reduction. *Phys. Fluids* **27** (9), 094103.

DOUAY, C. L., PASTUR, L. R. & LUSSEYRAN, F. 2016 Centrifugal instabilities in an experimental open cavity flow. *J. Fluid Mech.* **788**, 670–694.

DUGUET, Y., WILLIS, A. P. & KERSWELL, R. R. 2008 Transition in pipe flow: the saddle structure on the boundary of turbulence. *J. Fluid Mech.* **613**, 255–274.

EDWARDS, W. S., TUCKERMAN, L. S., FRIESNER, R. A. & SORENSEN, D. C. 1994 Krylov methods for the incompressible Navier–Stokes equations. *J. Comput. Phys.* **110** (1), 82–102.

FANI, A., CITRO, V., GIANNETTI, F. & AUTERI, F. 2018 Computation of the bluff-body sound generation by a self-consistent mean flow formulation. *Phys. Fluids* **30** (3), 036102.

FAURE, T. M., ADRIANOS, P., LUSSEYRAN, F. & PASTUR, L. 2007 Visualizations of the flow inside an open cavity at medium range Reynolds numbers. *Exp. Fluids* **42** (2), 169–184.

FAURE, T. M., PASTUR, L., LUSSEYRAN, F., FRAIGNEAU, Y. & BISCH, D. 2009 Three-dimensional centrifugal instabilities development inside a parallelepipedic open cavity of various shape. *Exp. Fluids* **47** (3), 395–410.

FISCHER, P. F., LOTTES, J. W. & KERKEMEIR, S. G. 2008 Nek5000 Web pages. http://nek5000.mcs.anl.gov.

FORTIN, A., JARDAK, M., GERVAIS, J. J. & PIERRE, R. 1997 Localization of Hopf bifurcations in fluid flow problems. *Intl J. Numer. Meth. Fluids* **24** (11), 1185–1210.

GIORIA, R. D. S., JABARDO, P. J. S., CARMO, B. S. & MENEGHINI, J. R. 2009 Floquet stability analysis of the flow around an oscillating cylinder. *J. Fluids Struct.* **25** (4), 676–686.

GLOERFELT, X. 2009 Cavity noise. *VKI Lecture Series* vol. 3, pp. 1–169.

HALL, K. C., THOMAS, J. P. & CLARK, W. S. 2002 Computation of unsteady nonlinear flows in cascades using a harmonic balance technique. *AIAA J.* **40** (5), 879–886.

HAMMOND, D. A. & REDEKOPP, L. G. 1997 Global dynamics of symmetric and asymmetric wakes. *J. Fluid Mech.* **331**, 231–260.

HWANG, Y. & COSSU, C. 2010 Linear non-normal energy amplification of harmonic and stochastic forcing in the turbulent channel flow. *J. Fluid Mech.* **664**, 51–73.

ITANO, T. & TOH, S. 2001 The dynamics of bursting process in wall turbulence. *J. Phys. Soc. Japan* **70** (3), 703–716.

JORDI, B. E., COTTER, C. J. & SHERWIN, S. J. 2014 Encapsulated formulation of the selective frequency damping method. *Phys. Fluids* **26** (3), 034101.

JORDI, B. E., COTTER, C. J. & SHERWIN, S. J. 2015 An adaptive selective frequency damping method. *Phys. Fluids* **27** (9), 094104.

KULIKOVSKII, A. G. 1966 On the stability of homogeneous states. *(Z. Angew. Math. Mech.) J. Appl. Math. Mech.* **30** (1), 180–187.

KUZNETSOV, Y. A. 1998 *Elements of Applied Bifurcation Theory*, Applied Mathematical Sciences, vol. 112. Springer.

LOISEAU, J.-CH. & BRUNTON, S. L. 2018 Constrained sparse Galerkin regression. *J. Fluid Mech.* **838**, 42–67.

LOPEZ, J. M., WELFERT, B. D., WU, K. & YALIM, J. 2017 Transition to complex dynamics in the cubic lid-driven cavity. *Phys. Rev. Fluids* **2** (7), 074401.

MALKUS, W. V. R. 1956 Outline of a theory of turbulent shear flow. *J. Fluid Mech.* **1** (5), 521–539.

MANTIČ-LUGO, V., ARRATIA, C. & GALLAIRE, F. 2014 Self-consistent mean flow description of the nonlinear saturation of the vortex shedding in the cylinder wake. *Phys. Rev. Lett.* **113** (8), 084501.

MANTIČ-LUGO, V., ARRATIA, C. & GALLAIRE, F. 2015 A self-consistent model for the saturation dynamics of the vortex shedding around the mean flow in the unstable cylinder wake. *Phys. Fluids* **27** (7), 074103.

MARQUES, F., LOPEZ, J. M. & SHEN, J. 2002 Mode interactions in an enclosed swirling flow: a double Hopf bifurcation between azimuthal wavenumbers 0 and 2. *J. Fluid Mech.* **455**, 263–281.

MAUREL, A., PAGNEUX, V. & WESFREID, J. E. 1995 Mean-flow correction as non-linear saturation mechanism. *Europhys. Lett.* **32** (3), 217–222.

MCKEON, B. J. & SHARMA, A. S. 2010 A critical-layer framework for turbulent pipe flow. *J. Fluid Mech.* **658**, 336–382.

MCMULLEN, M., JAMESON, A. & ALONSO, J. 2006 Demonstration of nonlinear frequency domain methods. *AIAA J.* **44** (7), 1428–1435.

MCMULLEN, M. S. & JAMESON, A. 2006 The computational efficiency of non-linear frequency domain methods. *J. Comput. Phys.* **212** (2), 637–661.

MELIGA, P. 2017 Harmonics generation and the mechanics of saturation in flow over an open cavity: a second-order self-consistent description. *J. Fluid Mech.* **826**, 503–521.

MELIGA, P., GALLAIRE, F. & CHOMAZ, J.-M. 2012 A weakly nonlinear mechanism for mode selection in swirling jets. *J. Fluid Mech.* **699**, 216–262.

MITTAL, S. 2008 Global linear stability analysis of time-averaged flows. *Intl J. Numer. Meth. Fluids* **58** (1), 111–118.

MORRIS, P. J. 1976 The spatial viscous instability of axisymmetric jets. *J. Fluid Mech.* **77** (3), 511–529.

PICELLA, F., LOISEAU, J.-CH., LUSSEYRAN, F., ROBINET, J.-CH., CHERUBINI, S. & PASTUR, L. 2018 Successive bifurcations in a fully three-dimensional open cavity flow. *J. Fluid Mech.* **844**, 855–877.

PIER, B. 2002 On the frequency selection of finite-amplitude vortex shedding in the cylinder wake. *J. Fluid Mech.* **458**, 407–417.

POLIASHENKO, M. & AIDUN, C. K. 1995 A direct method for computation of simple bifurcations. *J. Comput. Phys.* **121** (2), 246–260.

ROCKWELL, D. 1977 Prediction of oscillation frequencies for unstable flow past cavities. *Trans. ASME J. Fluids Engng* **99** (2), 294–299.

ROCKWELL, D. & KNISELY, C. 1980 Vortex-edge interaction: mechanisms for generating low frequency components. *Phys. Fluids* **23** (2), 239–240.

ROCKWELL, D. & NAUDASCHER, E. 1978 Self-sustaining oscillations of flow past cavities. *Trans. ASME J. Fluids Engng* **100** (2), 152–165.

ROSSITER, J. E. 1964 Wind tunnel experiments on the flow over rectangular cavities at subsonic and transonic speeds. *Tech. Rep.* Ministry of Aviation; Royal Aircraft Establishment; RAE Farnborough.

ROWLEY, C. W., COLONIUS, T. & BASU, A. J. 2002 On self-sustained oscillations in two-dimensional compressible flow over rectangular cavities. *J. Fluid Mech.* **455**, 315–346.

SCHMID, P. J. 2010 Dynamic mode decomposition of numerical and experimental data. *J. Fluid Mech.* **656**, 5–28.

SHANKAR, P. N. & DESHPANDE, M. D. 2000 Fluid mechanics in the driven cavity. *Annu. Rev. Fluid Mech.* **32** (1), 93–136.

SIPP, D. & LEBEDEV, A. 2007 Global stability of base and mean flows: a general approach and its applications to cylinder and open cavity flows. *J. Fluid Mech.* **593**, 333–358.

SIPP, D., MARQUET, O., MELIGA, P. & BARBAGALLO, A. 2010 Dynamics and control of global instabilities in open-flows: a linearized approach. *Appl. Mech. Rev.* **63** (3), 030801.

SMITH, J. O. 2007 *Mathematics of the Discrete Fourier Transform (DFT)*. W3K Publishing.

STUART, J. T. 1958 On the non-linear mechanics of hydrodynamic stability. *J. Fluid Mech.* **4** (1), 1–21.

SYMON, S., ROSENBERG, K., DAWSON, S. T. M. & MCKEON, B. J. 2018 Non-normality and classification of amplification mechanisms in stability and resolvent analysis. *Phys. Rev. Fluids* **3** (5), 053902.

THEOFILIS, V., DUCK, P. W. & OWEN, J. 2004 Viscous linear stability analysis of rectangular duct and cavity flows. *J. Fluid Mech.* **505**, 249–286.

TIESINGA, G., WUBS, F. W. & VELDMAN, A. E. P. 2002 Bifurcation analysis of incompressible flow in a driven cavity by the Newton–Picard method. *J. Comput. Appl. Maths* **140** (1–2), 751–772.

TUERKE, F., PASTUR, L., FRAIGNEAU, Y., SCIAMARELLA, D., LUSSEYRAN, F. & ARTANA, G. 2017 Nonlinear dynamics and hydrodynamic feedback in two-dimensional double cavity flow. *J. Fluid Mech.* **813**, 1–22.

TUERKE, F., SCIAMARELLA, D., PASTUR, L. R., LUSSEYRAN, F. & ARTANA, G. 2015 Frequency-selection mechanism in incompressible open-cavity flows via reflected instability waves. *Phys. Rev.* E **91** (1), 013005.

TURTON, S. E., TUCKERMAN, L. S. & BARKLEY, D. 2015 Prediction of frequencies in thermosolutal convection from mean flows. *Phys. Rev.* E **91** (4), 043009.

YAMOUNI, S., SIPP, D. & JACQUIN, L. 2013 Interaction between feedback aeroacoustic and acoustic resonance mechanisms in a cavity flow: a global stability analysis. *J. Fluid Mech.* **717**, 134–165.

YU, Y. H. 1977 Measurements of sound radiation from cavities at subsonic speeds. *J. Aircraft.* **14** (9), 838–843.

ZIELINSKA, B. J. A., GOUJON-DURAND, S., DUSEK, J. & WESFREID, J. E. 1997 Strongly nonlinear effect in unstable wakes. *Phys. Rev. Lett.* **79** (20), 3893.